Copper/Silver Bimetallic Nanoparticles Supported on Aluminosilicate Geomaterials as Antibacterial Agents

Published in: *ACS Applied Nano Materials*

Citation for published version: Cruces, E., Arancibia-Miranda, N., Manquián-Cerda, K., Perreault, F., Bolan, N., Azócar, M.I., Cubillos, V., Montory, J., Rubio, M.A., Sarkar, B., (2022) Copper/silver bimetallic nanoparticles supported on aluminosilicate geomaterials as antibacterial agents. *ACS Applied Nano Materials*. doi: 10.1021/acsanm.1c04031.

Document version: Accepted peer-reviewed version.

Copper/Silver Bimetallic Nanoparticles Supported on Aluminosilicate Geomaterials as Antibacterial Agents

Edgardo Cruces[a,b]*, Nicolás Arancibia-Miranda[b,c], Karen Manquián-Cerda[c], François Perreault[d], Nanthi Bolan[e,f], Manuel Ignacio Azócar[c], Victor Cubillos[g], Jaime Montory[h], María Angélica Rubio[b,c], Binoy Sarkar[i]*

[a] Centro de Investigaciones Costeras Universidad de Atacama (CIC-UDA), Avenida Copayapu 485, Copiapó, Chile

[b] Center for the Development of Nanoscience and Nanotechnology, CEDENNA, 9170124, Santiago, Chile

[c] Facultad de Química y Biología, Universidad de Santiago de Chile, Av. B. O'Higgins, 363, Santiago, Chile

[d] School of Sustainable Engineering and the Built Environment, Arizona State University, Tempe, AZ, USA

[e] School of Agriculture and Environment, The University of Western Australia, Perth, WA 6001, Australia

[f] The UWA Institute of Agriculture, The University of Western Australia, Perth, WA 6001, Australia

[g] Instituto Ciencias Marinas y Limnológicas, Universidad Austral de Chile, Valdivia, Chile

[h] Centro i~mar, Universidad de Los Lagos, Casilla 557, Puerto Montt, Chile

[i] Lancaster Environment Centre, Lancaster University, Lancaster, LA1 4YQ, United Kingdom

*Corresponding authors: edgardo.cruces@usach.cl (E. Cruces)

b.sarkar@lancaster.ac.uk (B. Sarkar)

Abstract

This work aims to understand how properties of modified aluminosilicate geomaterials influence the antibacterial performance of nanocomposites when prepared with bimetallic nanoparticles (NPs). Copper/Silver (Cu/Ag) bimetallic NPs were synthesized in the presence of imogolite (Imo), montmorillonite (Mtt) or zeolite (Zeo) using a simple one-pot method, and characterized for their crystal phases, micro- and nano-morphologies, particle size, elemental composition and electrophoretic mobility. The antibacterial activity was evaluated through minimum inhibition concentration assays of NPs and nanocomposites for Gram (-) *Escherichia coli*, and Gram (+) *Staphylococcus aureus* bacteria. Deposition of metallic Cu^0, Ag^0 and cuprite nanoparticles was confirmed in Zeo_Cu/Ag and Imo_Cu/Ag nanocomposites, whereas only Cu^0 and Ag^0 were identified in Mtt_Cu/Ag. The bimetallic NPs were more uniformly distributed on Zeo and Mtt than Imo. A particle size of 28.1 ± 5.0 nm, 9.4 ± 2.3 nm, 10.1 ± 1.7 nm and 12 ± 1.3 nm was determined for Cu/Ag NPs, Imo_Cu/Ag, Mtt_Cu/Ag, and Zeo_Cu/Ag, respectively. The release rate of Cu and Ag from Zeo_Cu/Ag was higher than pristine Cu/Ag NPs and other two nanocomposites. The antimicrobial action of bimetallic NPs and nanocomposites were dose-dependent in relation to the concentration of concerned materials and their stability in the medium. The physicochemical characteristics of Zeo resulted in a homogeneous distribution, and low oxidation and agglomeration of Cu/Ag NPs, consequently increasing the antibacterial activity. Results of this work highlight the benefits of using geomaterial support to achieve high antibacterial activity of bimetallic NPs, which could help reduce the consumption of pure Cu/Ag salts in NP-based antibacterial applications.

Keywords: Antibacterial activity; Cu/Ag bimetallic nanoparticles; Imogolite; Montmorillonite; Supported-nanoparticles; Zeolite.

1. Introduction

The antibacterial properties of metal and metal oxide (Ag, Cu, CuO, TiO_2, MgO, ZnO) nanoparticles (NPs) have received a widespread attention in recent years due to their capacity to serve as an alternative to conventional antibiotics for controlling pathogens [1,2]. The small size and high surface to volume ratio of NPs allow them to closely interact with bacterial cells, resulting in a higher antibacterial activity than the parent compound due to particle-mediated effects [3–5]. The high surface area of small particles also enhances the release of free metal ions from metal and metal oxide NPs, which contributes to bacterial inactivation [6]. The bactericidal mechanisms of NPs can be multi-fold, including the effects associated with oxidative stress induction, or non-oxidative mechanisms, such as the association of bacterial membranes and NPs through electrostatic attraction [7–9]. Often, these mechanisms act together to lead to bacterial inactivation. The specific mechanisms, however, depend on the properties and composition of the NPs concerned as well as their mode of exposure.

In particular, NPs made of Cu have been highlighted as promising antibacterial nanomaterials because of their potency against several microbial species, including Gram (+) and Gram (-) bacteria [10–12]. Although the mechanisms of antibacterial action are not fully elucidated, it is believed that Cu NPs can interact with the bacterial membrane and cause cell damage and bacterial inactivation [11,13]. The disruption of bacterial membranes and cell walls is associated with redox processes that occur between NPs and bacteria [7]. However, the oxidation of Cu NPs could result in a decrease in antibacterial activity by decreasing their reducing ability when interacting with bacterial surfaces [14]. Oxidation of metallic NPs' surface results in a conformational change in the NPs by forming a surface oxide layer. The spontaneous oxidation of Cu in the presence of atmospheric oxygen is thermodynamically favored, with ΔG^{o} = -130.12 kJ/mol and ΔG^{o} = -150.36

kJ/mol for Cu_2O and CuO, respectively. To solve this problem and improve the antibacterial property of metallic NPs, Lee et al. [15] proposed to incorporate a second metal on the structure, generating bimetallic NPs. The formation of Cu-Ag bimetallic nanoalloys was observed to reduce the access of oxygen, thus configuring more stable structures [16,17] and allowed for a slower release of ions than in monometallic conditions, both of which favored a synergy of action between the two metals [18–21]. However, the stability and size distribution of bimetallic NPs were found to be difficult to control, which impaired their antibacterial performance [22].

Immobilization of NPs on inert and stable materials, such as carbon nanomaterials [16], nanofibers [23,24], nanocellulose [25], silica nanotubes [21] or clay minerals [26] could prevent aggregation and preserve the antibacterial activity of NPs. In addition, the use of a support material during the synthesis of antimicrobial composites has the advantages of allowing for more precise size control, homogeneous distribution of NPs on the surface, or by acting as the reducing agents during NPs nucleation [27]. For example, Cu or Ag NPs supported on graphene oxide sheets, as a support for nucleation and stabilization, were found to have higher antimicrobial activity than the metallic particles alone [28,29]. The higher antimicrobial performance was attributed to a highest release of metal ions and a better stabilization of the metallic NPs [28,30]. Kim et al. [31] reported that the incorporation of Ag NPs on SiO_2, using a Stöber method to immobilize Ag on the SiO_2 surface, provided high antibacterial property of the composite material, which was related to the improved dispersion of NPs on the inorganic substrate that reduced aggregation of Ag NPs and enhanced the antibacterial performance. Natural clay minerals (*e.g.,* montmorillonite, halloysite) also possess several properties desirable for their use as a support during NP synthesis, such as high chemical and mechanical stability, varied surface and structural properties, high specific surface area, and good stability in aqueous media. Because of the natural availability and low cost, the

aluminosilicate geomaterials represent an excellent alternative to more expensive engineered materials, such as graphene, for the fabrication of antibacterial composites [32].

Aluminosilicate geomaterials such as montmorillonite (Mtt), imogolite (Imo), and zeolite (Zeo) have marked differences in their chemical composition, structure, and surface chemistry that provides support matrices for a wide variety of composite materials with different physicochemical properties, such as size, surface area, hydrophobicity, and surface charge. For example, Mtt is an expandable 2:1 type clay mineral whose laminar organization is characterized by two tetrahedral layers of silica and a central octahedral layer of alumina. Mtt has a net negative surface charge as a consequence of the isomorphic substitution of Si and Al in the layered structure occurred during the clay mineral formation. On the other hand, Imo is a nanotubular aluminosilicate presenting a high pH sensitivity to surface charge due to the aluminum groups (≡Al_2-OH and ≡Al-OH) predominating on the outer surface, and silanol groups (≡Si-OH) on the inner surface. Zeolite is a highly crystalline microporous aluminosilicates that, when dehydrated, form channels or pores with dimensions between 3 to 10 Å. The surface functional groups (≡Si-OH and ≡Al-OH) of Zeo provide some reactivity to pH variation, generally with an acidic isoelectric point (IEP). The three geomaterials above have different SiO_2/Al_2O_3 ratios, a parameter that determines their hydrophobicity (*e.g.*, Mtt > Zeo > Imo) [33,34]. The differences in hydrophobicity of the geomaterials would have a critical role in the behavior of NP-geomaterial composites and influence the bio-physicochemical interactions between the composite materials and biological systems.

In this study, we employed a simple one-pot synthesis method for bimetallic Cu/Ag NPs supported on three different geomaterials (Mtt, Imo and Zeo). This work aims to understand how the properties of the supporting geomaterials influence the antibacterial performance of

nanocomposites prepared with bimetallic NPs. The physicochemical properties of the different Cu/Ag NP-geomaterial composite materials, their ion release capacity in different media, and their antimicrobial activity as measured by minimum inhibition concentration towards Gram (-) (*Escherichia coli*) and Gram (+) (*Staphylococcus aureus*) bacteria were subsequently studied. This systematic approach will provide useful information on the optimal properties that enhance the antimicrobial capabilities of geomaterial-based nanocomposites.

2. Experimental Section

2.1. Reagents

All reagents were purchased and used as received from Sigma-Aldrich Co. LLC (St. Louis, MO, USA): copper (II) chloride hexahydrate ($CuCl_2 \cdot 6H_2O$; 99%), sodium borohydride ($NaBH_4$; 97%), aluminum chloride ($AlCl_3$; 99%), ammonia aqueous (NH_4OH. ACS reagent, 28 - 30%) and high purity silver nitrate ($AgNO_3$; ACS reagent, 99%). The Mtt clay mineral was acquired from Sigma-Aldrich and the Imo clay minerals was prepared using tetraethyl orthosilicate, ($Si(OC_2H_5)_4$; 99.995 %, Sigma-Aldrich), sodium hydroxide (NaOH; 99.996 %, Merck), and aluminium nitrate nonahydrate ($Al(NO_3)_3 \cdot 9H_2O$; 99.998 %, Merck) [35]. A natural Zeo, collected from a Chilean mine located at 36° 16′ S and 71° 40′ W, was ground, sieved through a 2 mm sieve and used in this study. HPLC grade ethanol was used as organic solvent and double-distilled water was used to prepare all the samples. Mueller-Hinton broth for bacterial inhibition experiments (MHB) was purchased from BiosChile (Difco). ASTM Artificial Seawater were purchased from Lake Products Company, USA.

2.2 Synthesis of Bimetallic Nanoparticles and Composite Materials

2.2.1. Synthesis of Cu/Ag Bimetallic NPs

Cu/Ag bimetallic NPs were prepared by a one-pot synthesis using $NaBH_4$ as a reducing agent. The synthesis was carried out at room temperature in a 500-mL borosilicate glass flask containing 400 mL of ethanol/H_2O solution (3:1) and 2.70 g $CuCl_2.6H_2O$ (0.7 mol of Cu). A $NaBH_4$ solution in excess (1.6 M) was added drop wise with constant mechanical stirring under an N_2 atmosphere (flow rate 50 mL min^{-1}) until a Cu/$NaBH_4$ ratio of 0.63 was reached and a black precipitate was observed. Then, 0.80 g of $AgNO_3$ (0.5 mol of Ag) was immediately added, resulting in a 2:1 Cu:Ag ratio. The choice of the Cu:Ag = 2:1 ratio was based on the lower Minimum Inhibitory Concentration (MIC) for *E. coli* in relation to different mass ratios of Cu and Ag used for the synthesis of bimetallic NPs (see Table S1). The reaction mixture was kept under agitation in an inert atmosphere (N_2, flow rate 50 mL·min^{-1}) for a period of 20 min. The resulting suspension was centrifuged at 9,000 rpm for 15 min (Sorvall RC-5C Plus, Kendro Laboratory Products, Connecticut, USA), and the supernatant was discarded. The black solid product was washed five times with an ethanol/ H_2O solution (3:1) using centrifugation (9,000 rpm for 30 min) each time to remove excess salts. The NPs were finally stored in a N_2-purged desiccator (Figure 1a).

2.2.2. Synthesis of Composites

To support the bimetallic NPs, geomaterials with different chemical reactivities as influenced by surface charge distribution were used, *i.e*., two variably charged geomaterials (Imo and Zeo) and one permanently charged clay mineral (Mtt). A synthetic Imo, prepared using our previously published procedure (Arancibia-Miranda et al., 2011) was used in this study. In brief: tetraethyl orthosilicate (TEOS) was added to a 5 mM aqueous solution of $AlCl_3$ until an Al:Si ratio

of 2:1 was reached. Then a 0.1 M NaOH solution was added at a rate of 1.0 $mL \cdot min^{-1}$ until an Al:Si:OH ratio of 2:1:4 was obtained. The mixture was stirred for 60 min and then heated at 368 K for 5 days. Once the aging process was completed, the resultant mixture was allowed to cool down to ambient temperature. A 0.1 M NH_4OH solution was added to the above mixture, stirring vigorously, until a pH of about 8.0 was reached. The solid was concentrated by centrifuging the suspension at 9,000 rpm for 30 min, and was washed with double distilled water until the discarded supernatant reached an electrical conductivity of less than 0.78 $S \cdot m^{-1}$.

Before preparing the composite materials (identified as Geomat_Cu/Ag), the geomaterials were homo-ionized with 0.1 M $NaNO_3$ for one week, to eliminate cations (Ca^{2+} and Mg^{2+}) that could hinder the Cu/Ag functionalization, and then freeze-dried. To prepare the composites with Imo, Mtt and Zeo, a mass ratio of Geomat: Cu: Ag = 6: 3: 1 was used**.** Thus, 1 g of aluminosilicate geomaterial was added into 500 mL methanol/water solution (3:1) and stirred for 2 h under an N_2 atmosphere (flow rate 50 $mL \cdot min^{-1}$). Then,1.340 g of $CuCl_2 \cdot 6H_2O$ dissolved in 400 mL of ethanol/H_2O solution (3:1) was added. Subsequently, $NaBH_4$ in excess (1.3% w/v) was added dropwise to the solution to achieve a final Cu/$NaBH_4$ ratio of 0.63. The solution was left under constant agitation and sonication for 10 min, maintaining a N_2 atmosphere. Then, 50 mL of a solution containing 0.4 g of $AgNO_3$ was added and stirred for 20 min in the inert atmosphere. Finally, the product obtained (black solid) was washed and centrifuged following the same procedure as for the bimetallic NPs (see section 2.2.1) (Figure 1b).

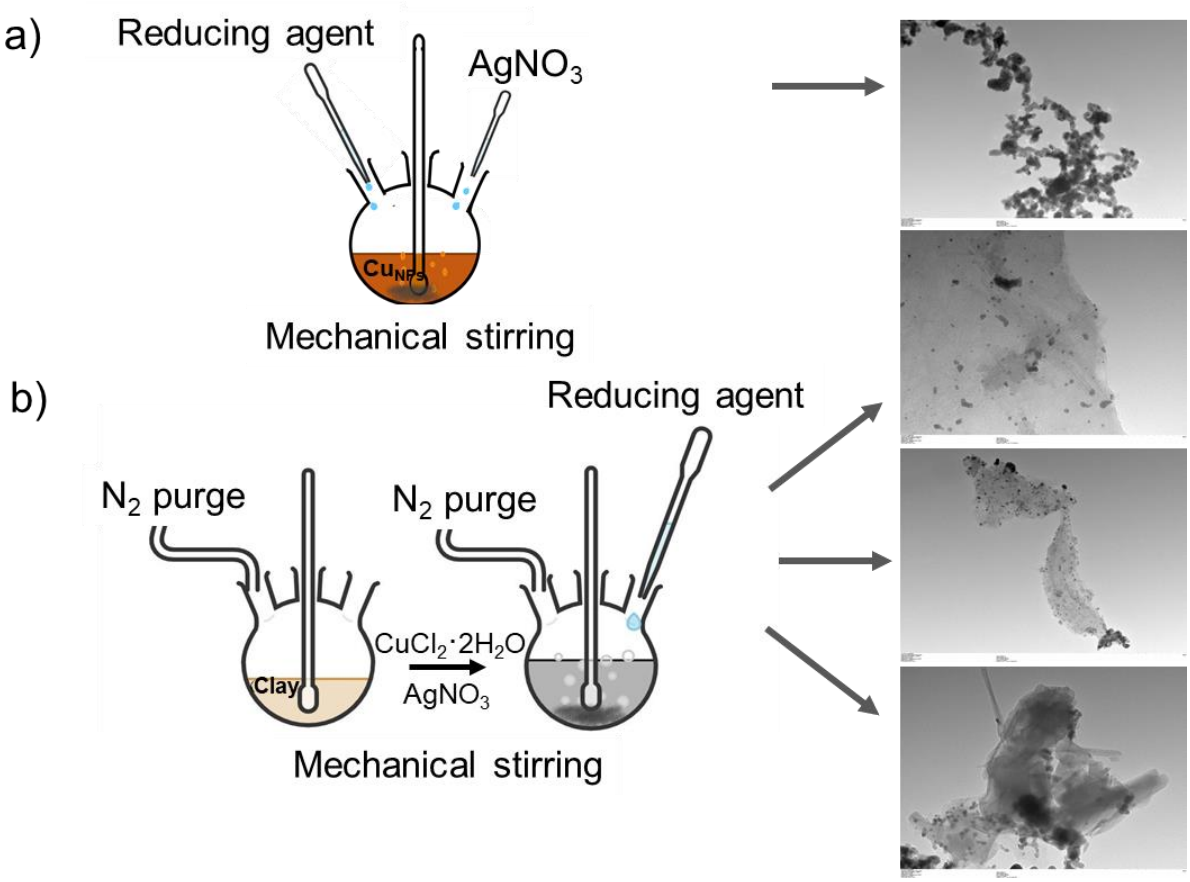

Figure 1. Preparation schemes for (a) Cu/Ag bimetallic NPs, and (b) NP-geomaterial composites.

2.3 Characterization of Synthesized NPs and Composites

The crystalline nature of the synthesized NPs and composites was determined by XRD analysis using a Shimadzu XRD-6000 diffractometer (Shimadzu Corporation, Tokio, Japan) with graphite-monochromated CuKα radiation, using oriented aggregate sample preparation procedure. Samples were obtained by drying water suspensions of the respective materials on glass slides. Morphological characterization and high-magnification images (>5000) were acquired with a backscattered electron (BSE) detector on an FEI Nova Nano-SEM 200 (Oregon, USA) scanning electron microscope (SEM) operated at 15 kV in a high vacuum. Elemental

analyses were performed using an INCA X-Sight energy dispersive X-ray spectrometer (EDS). The transmission electron microscopy (TEM) sample preparation was carried out by dipping Lacey Carbon Formvar-coated copper grids (300 Square, Pelco, USA) in a diluted suspension (ethanol/ H_2O solution (3:1) of samples. Then, the sample was dried in air prior to observation. Specimens were examined on a high-resolution transmission electron microscope (HRTEM) (Jeol JEM-2010F FE-TEM, Japan) with an accelerating voltage of 200 kV and a 0.19 nm point to point resolution. The isoelectric point (IEP) was determined by measuring the electrophoretic mobility (EM) of the particles on a Zeta Meter ZM4 apparatus (Zeta-Meter, Inc., USA). About 100 mg of each sample was suspended in 200 mL of a solution 1.0 mM (NaCl) background electrolyte. The IEP was obtained from the EM vs. pH graph as the pH at which EM = 0.

2.4 Elemental Analysis of NP and Composite Materials

The chemical composition of the geomaterials and composites after freeze-drying was analyzed by inductively coupled plasma atomic emission spectroscopy (ICP-AES) using a Perkin Elmer Optima 2000 equipment (Los Angeles, CA, USA). The samples (50 mg) were ground and dissolved in a mixture of 10% HNO_3 (1.0 mL) and HF (1.5 mL) solutions 24 h before the measurement. Each sample was measured 7 times, using Certipur® standards (Merck) corresponding to the main elements of concern (Al, Si, Cu and Ag).

2.5. Metal Release Studies

The release of Ag and Cu ions from the composites were measured up to 24 h of incubation in three different media: (i) distilled water (pH = 5.8±0.2), (ii) synthetic sea water (pH = 8.2±0.2), and (iii) Mueller-Hinton medium (pH = 7.4±0.2). Each composite (100 mg) was

immersed in 50 mL of the aqueous phase under continuous stirring (50 rpm). At various time intervals, 5 mL of release medium were sampled and the concentrations of released Ag and Cu ions were measured. The aliquot was dissolved with HNO_3 (1.0 mL, 10 % p/v) and stirred for 24 h, followed by ICP-AES analysis (Perkin Elmer Optima 2000) to determine total Ag and Cu concentrations [36]. For the determination of Cu and Ag, Certipur® standards were used. The quality of analysis on ICP-AES was verified by running standard samples at regular intervals (every ten samples). Standard curves for analysis were accepted with $R^2 > 0.9997$.

2.6. Determination of Antibacterial Activity

The bacteria *E. coli* (Gram (-), BW25113) and *S. aureus* (Gram (+), ATCC6538) (Universidad de Santiago of Chile) were grown at 37 °C overnight in a nutritive Müeller-Hinton (MHB) medium containing ($mg \cdot L^{-1}$): 2 beef extract, 17.5 casein acid hydrolysate, 1.5 starch, 17.0 agar, along with 1000 mL of distilled water. Then, in sterile 96-well plates, different volumes of culture medium were added along with increasing concentrations of nanomaterials (Cu/Ag NPs and nanocomposites) and double-distilled water until a uniform volume (80 µL) was achieved. To the above suspension, 20 µL of the bacterial inoculum grown overnight and diluted to a McFarland = 0.5 (approximately 5×10^5 $CFU \cdot mL^{-1}$) was added. In addition, appropriate sterile controls were performed: Mueller-Hinton culture medium alone, and Mueller-Hinton culture medium plus bacterial inoculum (*E coli*, and *S. aureus*). Finally, the plates were incubated at 37°C for 24 h, and the absorbance at 600 nm was determined in an Elisa reader (Thermos Labsystems Multiskan GO Model, BioTek Instruments, Inc., USA). The concentrations of the different nanomaterials used were as follows: 6.25, 12.5, 25, 50 and 100 $mg \cdot L^{-1}$. Absorbance was measured at 1 h interval over 24 h, with time zero being the moment at which the medium was inoculated. At each

absorbance value, measured at 600 nm, the absorbance of the corresponding suspension of nanomaterials (MHB + composites) was subtracted, and growth control (MHB + inoculum) was considered as 100% growth of bacteria.

Metal(loid) toxicity to microorganisms including bacteria is also often expressed as lethal concentration (LD_{50}), effective concentration (EC_{50}) or MIC. The LD_{50} and EC_{50} values represent the metal(loid) concentration at which the bacterial growth is reduced by 50% of the growth obtained for the control treatment in the absence of metal(loid) input. The MIC value represents the minimum metal(loid) concentration at which the bacterial growth is completely inhibited.

The net concentration of Cu/Ag in each nanocomposite (Imo_Cu/Ag, Mtt_Cu/Ag and Zeo_Cu/Ag) necessary to inhibit *E. coli* and *S aureus* growth was calculated using the following formula (Eq. 1):

$$NC = \frac{MICx\ NPs\%}{100} \quad (Eq. 1)$$

where, NC is net concentration of Cu/Ag in each nanocomposite ($mg \cdot L^{-1}$), MIC is the minimum inhibition concentration of each nanocomposite necessary to inhibit bacterial growth over 24 h, and NPs% is the percentage of metal (Cu and Ag) present in each nanocomposite according to ICP-AES analysis with respect to one gram of sample (see Table 1).

3. Results and Discussion

3.1. Synthesis and Characterization of NPs and Composites

A simple one-pot synthesis method was employed for the formation of Cu-Ag bimetallic nanoalloys. The synthesis procedure in this study used $NaBH_4$ as a reducing agent to achieve simultaneous co-reduction of both the metals[20]. A similar experimental protocol used earlier by Sepúlveda et al [37] confirmed the synthesis of bimetallic NPs with non-uniform core-shell

structures. The geomaterials used were structurally different and provided various amounts of permanent and variable charges, which conditioned the synthesis and reactivity of Cu/Ag NPs [38,39]. Ferrando et al.[17] showed that, according to the chemical nature of the metals used, the synthesis of bimetallic NPs might depend on a number of factors. The factors that determine the eventual order of the bimetallic NPs formation are: relative strength of the bond, surface energy of the metals, relative atomic size, charge transfer, and specific electronic/magnetic effect [17]. The formation of bimetallic NPs in this work was deduced from the XRD, SEM-EDS and TEM characterization results.

3.1.1. X-ray Diffraction Patterns of Synthesized Materials

The materials synthesized in this study (Cu/Ag bimetallic NPs and composites) were characterized with respect to their crystal phase structure using XRD. Figure 2 shows the X-ray diffractograms of pristine Imo, Zeo, Mtt, Cu/Ag NPs, and Geomat_Cu/Ag. The crystal structural conformation of bimetallic NPs allowed their diffraction planes to be sharper, giving intense reflections, whereas geomaterials, being a more complex structure than pure NPs, gave decreased signals for respective phases. The changes in reflection intensities in the patterns of Geomat_Cu/Ag could be due to a dilution effect, which was related to the ratio of NPs imbedded in different geomaterials. The diffractogram of Cu/Ag NPs identified different reflections associated with metallic Cu^0 (at 2θ = 43.3°, 50.2°, and 73.9°), while the reflections for Ag^0 were detected at 2θ = 38.1°, 44.0°, 64.5° and 77.4°, highlighting the interaction of Ag NPs with the surface of the Cu NPs due to the fact that both metals have the same structural ordering (face centered cubic (FCC) ordering). Few reflections associated with cuprite (Cu_2O) were also detected with low intensity (Figure 2), likely due to a partial oxidation of Cu during the synthesis

of Cu/Ag NPs in the absence of geomaterials. In the diffractogram of Imo, three diffuse reflections were observed at 2θ = 8.2°, 26.5° and 40.3° as a consequence of the para-crystalline structure of the material, which are characteristics of a monoclinic order or hexagonal arrangement of the crystal structure [35]. The diffractogram of Zeo indicated that the sample was an Al-mordenite type zeolite, with reflections at 2θ = 20.0, 26.4, 27.7 and 30.8° (the corresponding d values were 4.44, 3.38, 3.22 and 2.90 Å, respectively) [33]. An impurity of quartz was detected in the Zeo sample, with a reflection found at 2θ = 27.3°. The diffractogram of Mtt showed reflections at 2θ = 7.6°, 22.4°, 28.4°, 35.3°, 37.8°, 54.4° and 62,3° (d value = 12.5, 4.45, 3.34, 3.16, 2.55, 1.69 and 1.50 Å, respectively), which corresponded to a mixture of various minerals, including Na–Mtt ($Na_{0.3}(Al,Mg)_2Si_4O_{10}\cdot 8H_2O$) (85%), muscovite ($KAl_2(Si_3Al)O_{10}(OH,F)_2$) (9%), and Illite–Mtt ($KAl_4(Si,Al)_8O_{10}(OH)_4\cdot 4H_2O$) (6%).

The one-pot synthesis of Cu/Ag NPs over the geomaterials significantly changed the diffraction patterns of the composites (Fig. 2). In the diffractogram of Imo_Cu/Ag, significant changes were determined in the degree of crystallinity, observing an attenuation of the Imo reflections, as a consequence of the functionalization process with Cu/Ag NPs. The functionalization of Imo with Cu/Ag NPs showed highly crystalline reflections associated with the presence of Cu^0 and Ag^0, in addition to a less intense Cu_2O reflection, accounting for a partial oxidation of Cu^0. The diffractogram of Zeo_Cu/Ag showed Cu/Ag reflections similar to those described for Imo_Cu/Ag, establishing the presence of crystal phases of Cu^0 and Ag^0 and cuprite (Fig. 2), with reflections at 2θ = 20.0, 26.4, 27.7 and 30.8° (the corresponding d values were 4.44, 3.38, 3.22 and 2.90 Å, respectively). In the diffractogram of Mtt_Cu/Ag, reflections associated to Cu^0 and Ag^0 and Mtt were identified, demonstrating the effectiveness of Mtt in the synthesis of the composite material. A displacement of reflection position from 2θ = 7.6° to 8.8° (d value 11.35

to 9.81) in Mtt_Cu/Ag was detected, which corresponds to the intercalation of Cu^{2+} or Ag^{+} during the synthesis process of Cu/Ag NPs, where the guest cations would have displaced Na^{+} from the clay interlayer, causing the basal distance to decrease, a phenomenon reported in the literature [39,40].

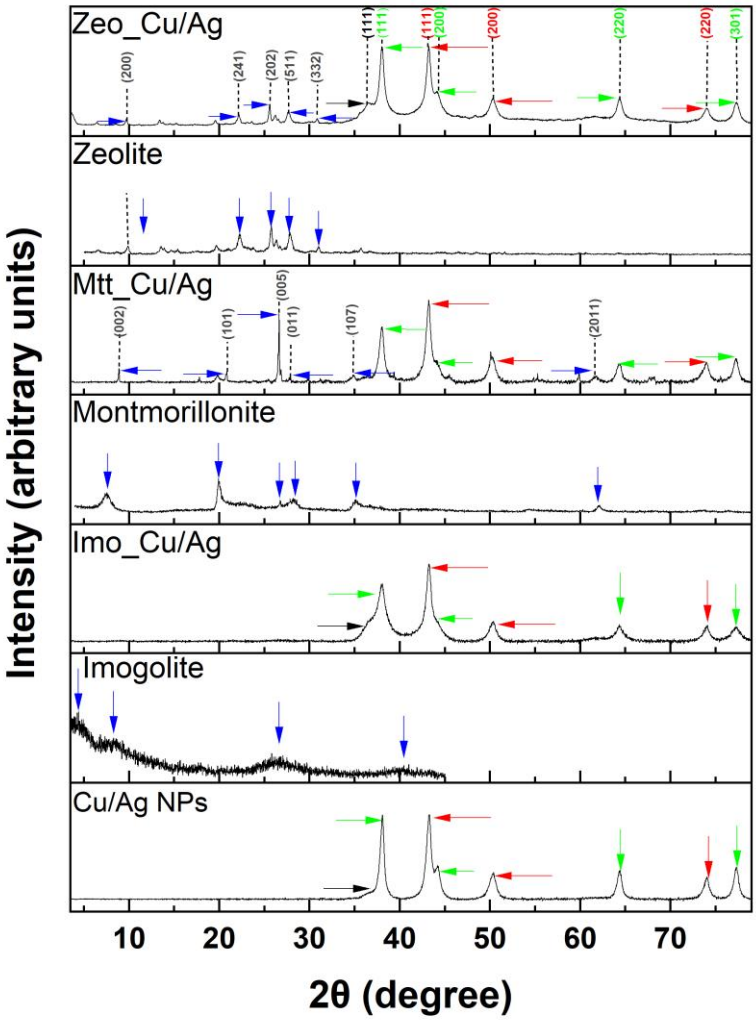

Figure 2. XRD patterns of pristine geomaterials, bimetallic NPs and their composites. The colors of the arrows indicate the different crystalline phases detected (green = metallic Ag (JCDPDS No. 04-0783); red = metallic Cu (JCDPDS No. 04-0836); black = cuprite (JCDPDS No. 05-0667), and blue = characteristic reflections of the geomaterials). Note: In the Imo_Cu/Ag diffractogram, the imogolite reflections are strongly attenuated due to the high reflection intensity of Cu/Ag NPs.

3.1.2. Characterization by Scanning and Transmission Electron Microscopy

The presence of cuprite (Cu_2O) was detected in Cu/Ag NPs, Imo_Cu/Ag and Zeo_Cu/Ag, but not in Mtt_Cu/Ag, likely due to the different structures and charge behaviors of the geomaterials. In Imo_Cu/Ag the small internal tube diameter (~1.0 nm) might have restricted the diffusion of Cu^{2+} and Ag^{+} ions inside the geomaterial [41], which could happen also in Zeo_Cu/Ag due to small pore size of Zeo [33]. Therefore, the adsorption of Cu^{2+} and Ag^{+} ions on Imo and Zeo occurred mainly on the external surface, where Cu of Cu/Ag NPs was subjected to partial oxidation [41]. This oxidation phenomenon was also evident in the TEM micrographs (Fig. 4. a1, a2), where an agglomerate of NPs in the form of a chain was seen in the case of Cu/Ag NPs, as a consequence of the formation of -OH groups on the surface external of these materials, which favors interactions of the hydrogen bridge type [37]. In contrast, the TEM image of Mtt_Cu/Ag showed sheet-like structure of Mtt allowing Cu^{2+} and Ag^{+} ions first to be entered in the interlayer space through cation exchange process and then converted to Cu^0/Ag^0 NPs. Protection of the NPs within the Mmt interlayer space restricts contact with dissolved O_2 during synthesis, leading to only Cu^0 (not Cu oxides) being found in the bimetallic NPs stabilized on Mtt [32].

The morphology of the synthesized materials was studied by SEM and TEM. The SEM image of Cu/Ag NPs (Figure 3.a) showed an irregular spherical morphology for the NPs, with high agglomeration generated by the surface oxidation of the nanomaterials and the formation of cuprite, which was detected by XRD analysis. This phenomenon was further confirmed by TEM images (Figure 4. a1, a2), where areas of different electronic density were observed in the bimetallic Cu/Ag NPs, suggesting that Cu_2O was likely present on the surface of these NPs. The NPs presented chain-like structures due to the presence of Cu_2O generated during the synthesis,

which is thermodynamically favored [42]. The particle diameter was estimated from an average of 20 measurements ($p < 0.05$, t test, sample size 20 NPs) at different scales and defined by a high-resolution analysis of the images. The average diameter of Cu/Ag NPs was determined from TEM photomicrographs to be 28.1 ± 5.0 nm. In the case of the composites, the geomaterial structure caused a decrease in the size of the bimetallic NPs immobilized on the geomaterial surfaces. In Figure 3.b, the SEM image of Imo_Cu/Ag revealed agglomerated Cu/Ag NPs, with a particle size of 9.4 ± 2.3 nm. The TEM image (Figure 4. b1, b2) showed that the distribution of Cu/Ag NPs in Imo was mainly at the end of the nanotubes. This behaviour had its origin in the surface charge of Imo, where the positive charge of Imo under the synthesis conditions formed an electrostatic barrier limiting homogeneous adsorption of Cu^{2+} and Ag^{+} ions on the entire Imo surface [43]. The Cu^{2+} and Ag^{+} ions were rather adsorbed on specific surface sites at the end of the tubes (negatively charged) [41,44], generating attraction nuclei for NP growth. The above sites would be found at the edges of the nanotubes since they were the ones with the highest sensitivity to pH change. The SEM image of Mtt_Cu/Ag (Figure 3. c) showed that the NPs were distributed homogeneously on the surface of the clay mineral, suggesting greater interaction with the surface than in the case of Imo and Zeo. TEM analysis of Mtt_Cu/Ag (Figure 4. c1, c2) further confirmed the homogeneous distribution of Cu/Ag NPs on the clay mineral surface, less particle aggregation, and an average size of particles of 10.1 ± 1.7 nm. For the Zeo_Cu/Ag system (Figure 3. d), the Cu/Ag NPs were distributed with a high homogeneity on the surface of the Zeo, which could be a consequence of the negative surface charge that Zeo had, which will be discussed later. The size distribution of the Zeo_Cu/Ag, determined by TEM photomicrographs (Figure 4. d1, d2), showed that the Cu/Ag NPs had a diameter range of 10 to 35 nm, with a mean value of 12.2 nm. The differences observed between the Imo, Mtt and Zeo composites were related to the surface

charge of the respective geomaterial, which determined the type of interaction between the surface-active groups and the metal cations present.

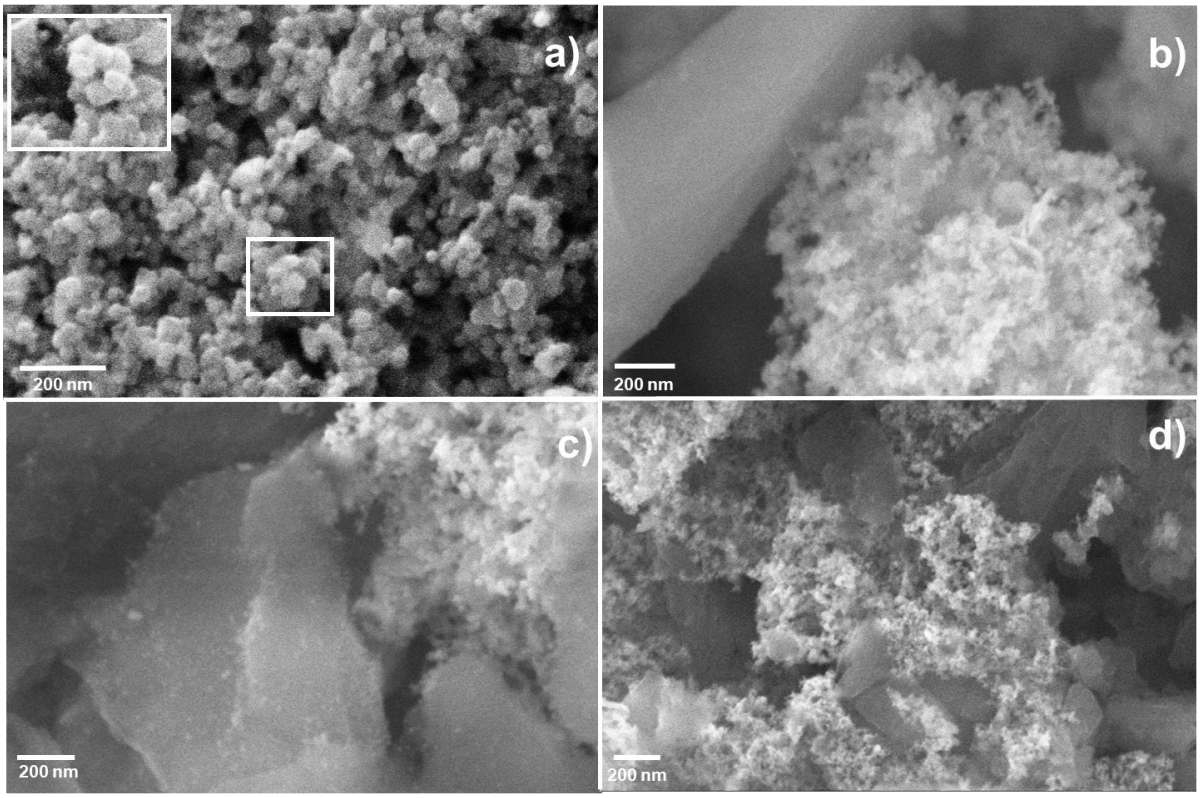

Figure 3. SEM images of Cu/Ag bimetallic NPs (a), Imo_Cu/Ag (b), Mtt_Cu/Ag (c) and Zeo_Cu/Ag (d). Inserts in (a) is an enlarged picture of Cu/Ag NPs structure.

The characterization of different regions of the samples by SEM-EDS showed the presence of different elements. In Cu/Ag bimetallic NPs (Figure S1a), the EDS spectrum showed the presence of Cu, Ag and O, likely associated with the presence of cuprite in this material, as discussed above. The EDS analysis of Imo_Cu/Ag showed high percentage of metal associated with other elements such as Al, Si, Na (Figure S1b). The high percentage of O was associated with the Imo structure as well as to the oxidation of Cu/Ag NPs, while Na was associated with the

residual salt of precursor reagents used in the synthesis of Imo. The EDS of the Zeo_Cu/Ag identified elements associated with Zeo such as Si, Al, Fe, K and O, in addition to Cu and Ag corresponding to the functionalization of Zeo with the bimetallic NPs (Figure S1d). Likewise, in Mtt_Cu/Ag (Figure S1c), the EDS spectrum revealed the presence of O, Si, Al, Fe, K, Ti, Na, and Mg associated to Mtt, as well as Cu and Ag from bimetallic NPs. In all the materials, the percentage of Cu and Ag were consistent with the mass ratio Cu/Ag proposed in this work (Figure S1).

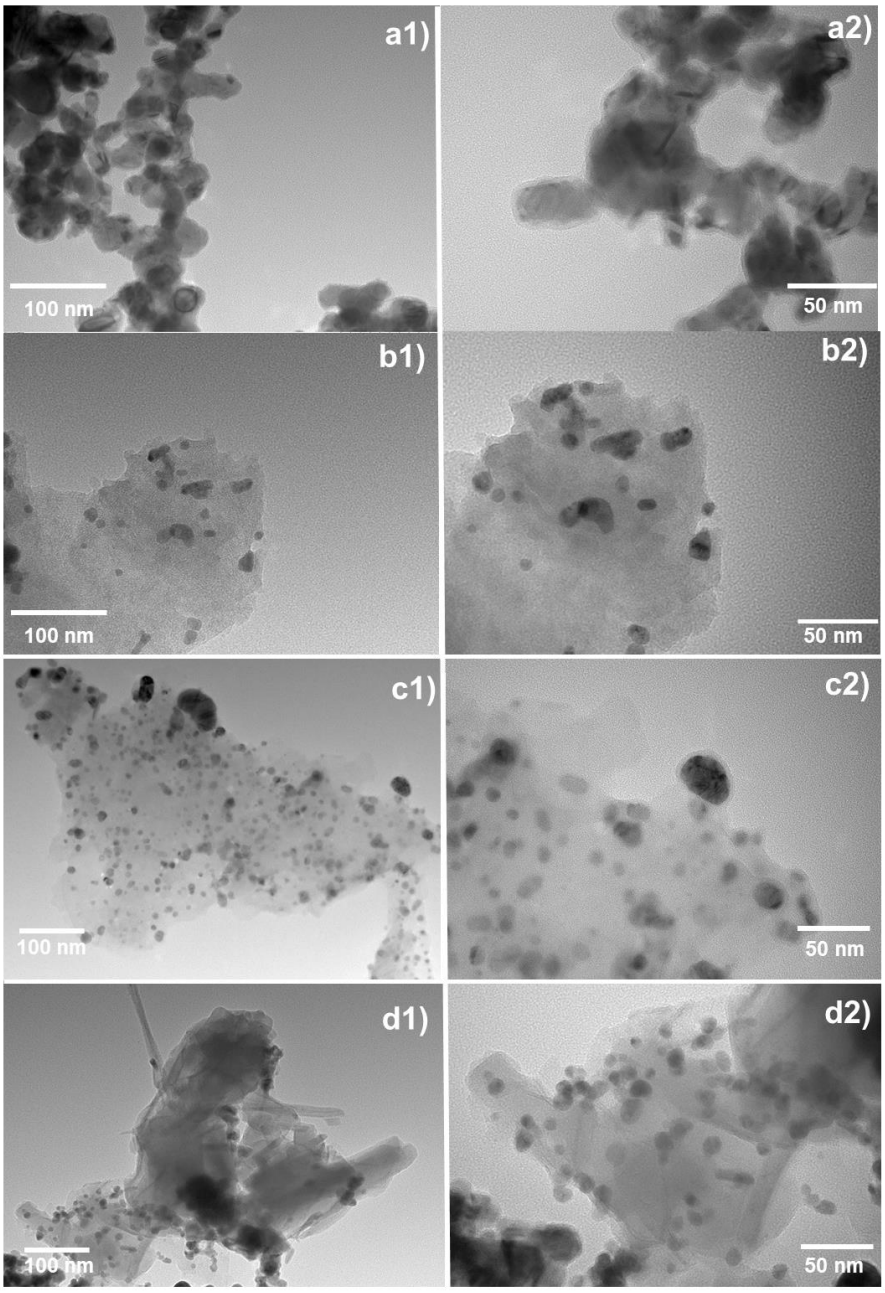

Figure 4. TEM images of Cu/Ag bimetallic NPs (a1 and a2, respectively), Imo_Cu/Ag (b1 and b2, respectively), Mtt_Cu/Ag (c1 and c2, respectively) and Zeo_Cu/Ag (d1 and d2, respectively).

3.1.3. Electrophoretic Characterization

In order to obtain information on the surface chemistry of the different materials, the zeta potential (ZP) was measured as a function of pH (Figure 5). The different geomaterials were found to have different electrokinetic behaviors; in the case of Zeo and Mtt, the surface charge was negative over a wide pH range. The IEP of Zeo was observed around 2.9 while no IEP was found for Mtt (Figure 5a). The Imo contrasted with the other two geomaterials used in that had by a positive charge over a wide pH range and an IEP = 9.5, above which the surface was negatively charged. Under most environmentally relevant conditions, Imo will be positively charged (Figure 5a). The Zeta potential characterization of the three geomaterials used in this study concurs with those reported by Arancibia-Miranda et al. [33] and by Arancibia Miranda et al. [45]. In the case of Cu/Ag NPs, an IEP value was not observed, and the surface charge was always negative throughout the studied pH range (Figure 5b). The addition of Cu/Ag NPs on the geomaterials did not generate significant changes in the electrokinetic behavior of Zeo_Cu/Ag and Mtt_Cu/Ag, with only a slight increase in the ZP values of both composites compared to the pristine geomaterials potentially attributed to the net negative surface charge of the NPs (Figure 5b). However, for Imo_Cu/Ag, in addition to observing a decrease in the magnitude of the charge, the IEP value shifted to a more acidic pH value (IEP = 8.7). This shift may be attributed to the functional groups of the Cu/Ag NPs, which are more acidic than the Al-OH groups in pristine Imo (Figure 5b) [45,46].

The ZP values of all the materials were determined in the culture medium (MHB) (pH ~7.4) used in the antibacterial activity studies and compared with the measurements made in NaCl (1.0 mM) as a background electrolyte. A significant decrease in the ZP value of Imo and Imo_Cu/Ag was observed in the MHB culture medium, where the values were 18 ± 1 mV for Imo and 13 ± 2 mV for Imo_Cu/Ag, being approximately 50% lower than observed in NaCl. This change can be

related to the interaction of Imo and Imo_Cu/Ag with casein hydrolysate in MHB. Casein hydrolysate would be negatively charged at pH = 7.4±0.2, favoring its adsorption on the surface of Imo and Imo_Cu/Ag. In MHB, the ZP values of Cu/Ag_NPs, Zeo_Cu/Ag and Mtt_Cu/Ag were -11 ± 1, -19 ± 2, and -23 ± 1 mV, respectively, observing a decrease in the ZP values of composites compared to the pristine geomaterials, although not in the magnitude of ZP for Imo_Cu/Ag. The above variation in ZP was due to the immobilization of NPs on geomaterials and their chemical nature. However, since the net surface charge of Zeo and Mtt was negative, they did not significantly interact with casein hydrolysate in MHB, giving lesser variation of ZP values by their composites compared to Imo_Cu/Ag.

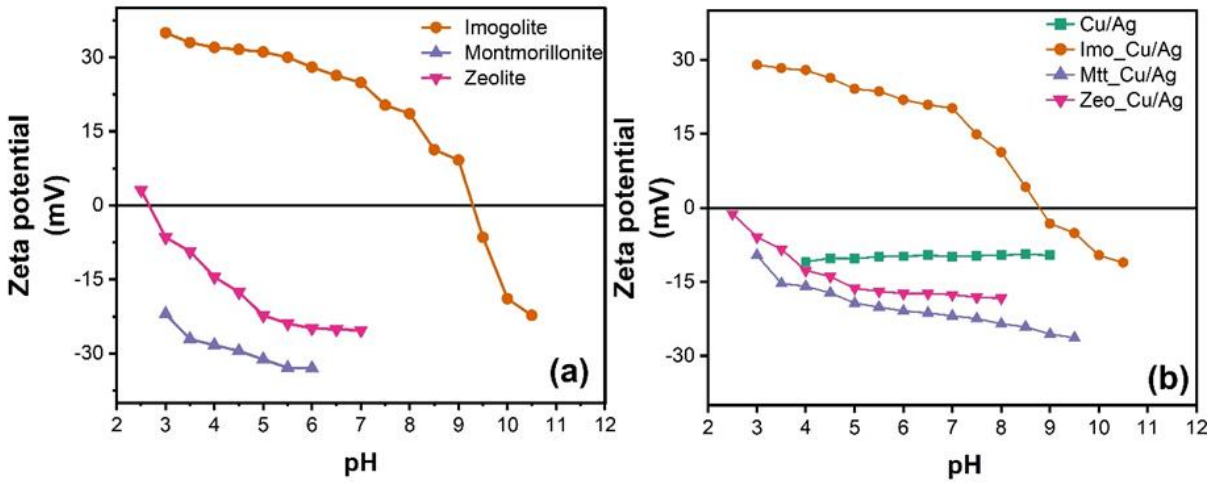

Figure 5. Zeta potential values of geomaterials (a) and synthesized bimetallic NPs supported on the geomaterials (b), as affected by pH.

3.2. Elemental Composition of Bimetallic NPs, Geomaterials and Composites

The total elemental contents of the NPs, geomaterial and composite samples are summarized in Table 1. According to the ICP-AES analysis, the pristine Mtt and Zeo contained 4

to 6% of Cu, and 3 to 3.5% of Ag, respectively, due to the natural origin of these elements in the geomaterials. In the case of Imo, Cu and Ag were not detected, because the reagents used in their synthesis did not contain the concerned elements. After synthesis, the Cu and Ag content of the Geomat_Cu/Ag composites increased to by ~300 $mg \cdot g^{-1}$ and ~100 $mg \cdot g^{-1}$, respectively, with small variations based on the nature of the geomaterial support. Subtracting the background Cu and Ag naturally occurring in the support, the Cu/Ag particles formed on the different composites were found to have a Cu:Ag ratio of 3.24, 3.01, and 2.86, for Imo_Cu/Ag, Mtt_Cu/Ag, and Zeo_Cu/Ag, respectively. The SEM-EDS spectral analysis showed Cu:Ag ratio of 3.3, 2.8 and 2.6 for Imo_Cu/Ag, Mtt_Cu/Ag and Zeo_Cu/Ag, respectively (Figure S1), reiterating the ICP-AES results. These results indicate a lower silver content for the Geomat_Cu/Ag composites than in the Cu/Ag NPs, which have a Cu/Ag ratio of 2.03. The difference in Cu/Ag ratio in the Geomat_Cu/Ag composites does not appear related to the distribution of the particles on the geomaterial support, since Imo_Cu/Ag and Zeo_Cu/Ag both have Cu/Ag NPs nucleated on the support. Rather, silver loading in the Geomat_Cu/Ag composite is more correlated with ZP, with more negative surface charge resulting in higher Ag content.

Table 1. Chemical composition of geomaterials, Cu/Ag NPs and their supported composites. Data are mean ± SD, $n = 3$.

Samples	Cu	Ag	Si	Al
	(mg·g^{-1})			
Cu/Ag NPs	670 ± 56	329 ± 33	ND	ND
Imo	ND	ND	142 ± 12	272 ± 25
Mtt	40 ± 1	30 ± 1	311 ± 24	149 ± 15
Zeo	60 ± 2	35 ± 3	60 ± 6	314 ± 28
Imo_Cu/Ag	301 ± 21	93 ± 9	85 ± 3	164 ± 5
Mtt_Cu/Ag	333 ± 33	127 ± 14	187 ± 11	88 ± 7
Zeo_Cu/Ag	358 ± 15	139 ± 9	37 ± 1	190 ± 6

3.3. Release of Silver and Copper Ions from Composites

The release of Cu and Ag from the different materials was considered for different time intervals (2, 6, 12 and 24 h) in the following media: distilled water (DW), MHB medium (MHB), and seawater (SW). In general, the percentage release of Ag from all materials was higher than that of Cu, especially in the first 2 h in both DW and MHB, and then maintaining the same pattern as that of Cu throughout the experiment. In the case of SW, due to high ionic strength, the release of Ag and Cu was faster and more intense, making it challenging to determine the difference in metal release pattern in SW. The metal release kinetics of NPs were governed by their particle size and physicochemical parameters of the medium such as ionic strength, pH and dissolved organic carbon content.

A difference in the behavior of Cu and Ag release was observed as a function of the geomaterials used in the composites (Figure 6). The immobilization of Cu/Ag NPs on a geomaterial support matrix reduces agglomeration and increases the contact surface, thus favoring metal release over time. However, in the case of Cu/Ag and Imo_Cu/Ag NPs (Figure 6),

a similar release pattern was seen with only, slightly higher metal release from the composite. This can be attributed to the structure of the Imo geomaterial and its impact on the Cu/Ag immobilization. In Imo_Cu/Ag, the Cu/Ag NPs are mainly located at the edges of the Imo tubular structure because the diffusion of metal ions towards the inner surface of the nanotube is restricted [41] (Figure 3d). This results in aggregation of NPs in Geo_Cu/Ag composite, similar to unsupported NPs. Another critical effect to consider in the Imo_Cu/Ag composite is the high sensitivity of Imo to factors such as pH and ionic strength, which may favor the aggregation process when environmental conditions are changed [47].

For Zeo_Cu/Ag and Mtt_Cu/Ag, a high release of Cu and Ag over time was observed when compared to Cu/Ag NP and Imo_Cu/Ag (Figure 6). This behavior might be a consequence of the physicochemical properties of both Zeo and Mtt. The negative surface charge of Zeo and Mtt favored a more homogeneous distribution of Cu/Ag NP on the geomaterial surface, which facilitated a steady release of Cu and Ag ions over time. The structural differences between Zeo and Mtt influence how these geomaterials release Cu^{+} and Ag^{+} ions. For example, the layered structure of Mtt possibly results in the intercalation of both metals,–leading to the eventual oxidation of the NPs and a decrease in their dissolution [40,48]. Oxidation of Cu was confirmed in this study by XRD (Figure 2). In the case of Zeo, the distribution of Cu/Ag NPs on its surface, the structural stability and their pore size (<2 nm [49]; would enhance the release of ions through the Zeo matrix to the external surface. The ICP-AES analysis showed ~40% total Cu/Ag content in Geo_Cu/Ag. However, the metal release pattern showed a maximum release occurred in about 24 h, reaching only ~22% of the total metal present in the nanocomposites. This fast releasing fraction could be attributed primarily to the metal fraction embedded on the surface of the nanocomposites.

The release pattern of Cu and Ag from the materials suggested that the process was dependent on the electrochemical potential of the suspension, pH, ionic potential of the aqueous medium, exposed surface area, distribution of NPs in the composites, and nature of each element that constituted the NPs [7,50]. During the first hour of contact of the materials with aqueous solutions (DW, MHB, and SW), an "ionic burst" of both Cu and Ag occurred, with greater than 50% of the total metal release (Figure 6). This initial fast release could have its origin in the corrosion and dissolution of Cu/Ag NPs that were the most exposed to the aqueous environment, such as those located on the edges of the geomaterials [50]. However, from 1 h onwards and up to 12 h of contact, a continuous slow release of metal ions was observed, lower in magnitude than the initial burst, for all the composites. This stage would be related to the release of ions from Cu/Ag NPs located inside the geomaterial structure or pores that had less access to the external environment, causing metal release to be delayed. Based on the results of this study, the decreasing order of release of Cu and Ag ions after 24 h was as follows: Zeo_Cu/Ag ≥ Mtt_Cu/Ag > Imo_Cu/Ag > Cu/Ag.

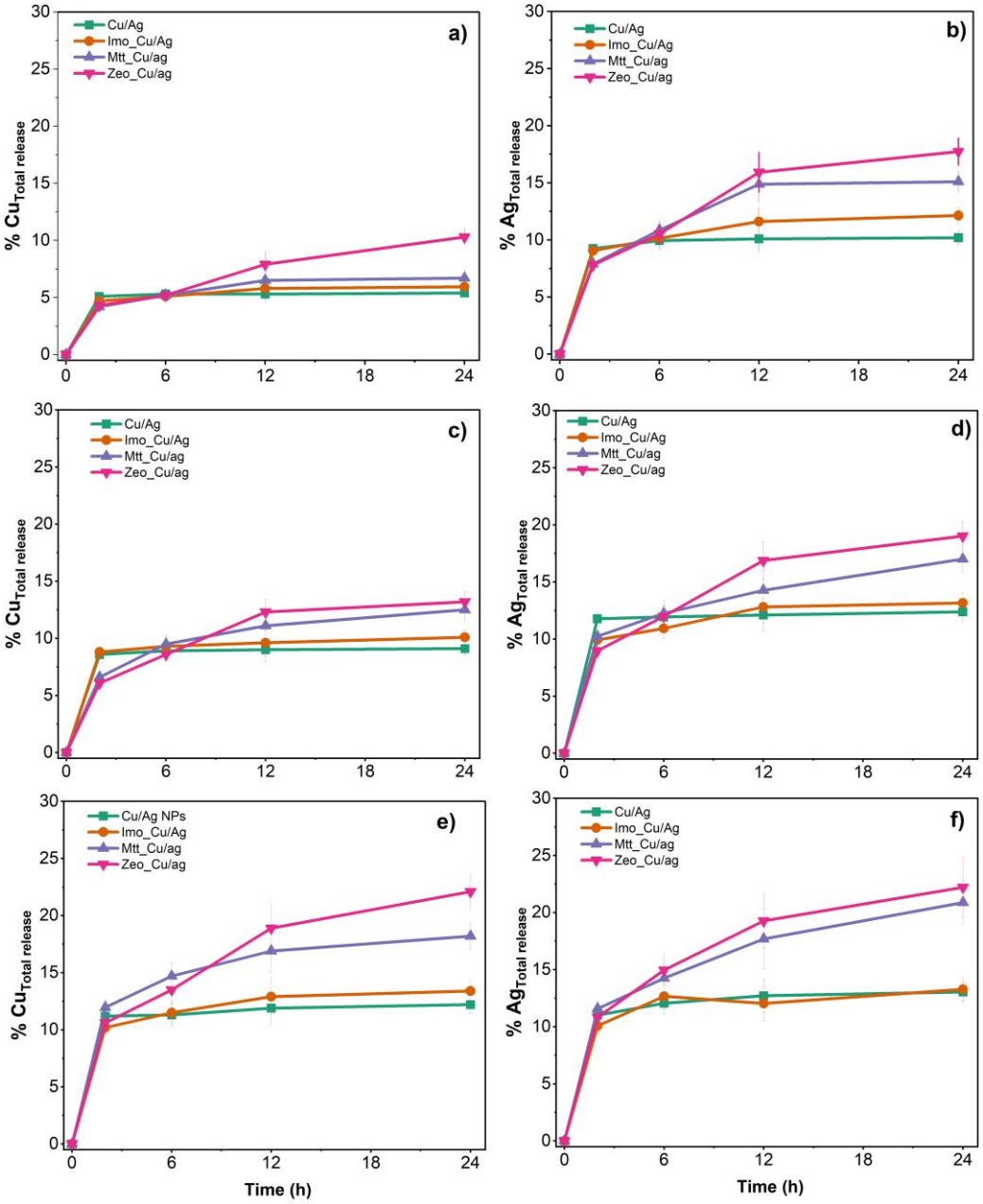

Figure 6. Cumulative release percentages of Cu and Ag ions from Cu/Ag NPs, Imo_Cu/Ag, Mtt_Cu/Ag and Zeo_ Cu/Ag composites in distilled water (DW) (a and b), Müeller-Hinton Broth (MHB) medium (c and d), and seawater (SW) (e and f) at time intervals of 2, 6, 12 and 24 h.

3.4. Effect of Nanocomposite on Bacterial Growth Inhibition

The effect of Cu/Ag bimetallic NPs on the inhibition of growth of *E. coli* and *S. aureus* was governed mainly by the concentration of NPs. During the first 12 h of incubation, the minimum NP concentration needed to inhibit 100% (MIC) of the bacterial growth varied between 6.25 and 12.5 $mg \cdot L^{-1}$, increasing to up to 25 $mg \cdot L^{-1}$ in both strains at 24 h (Figure 7a, 7b). A high concentration of bimetallic NPs increased the toxicity due to either a higher concentration of Cu^{2+} and Ag^{+} ions in the medium or from the direct action of NPs in contact with the surface of the bacteria [3,51] (Figure 6, Figure 7a, 7b). Considering the concentrations of Cu and Ag used in each composite (Table 1), the release experiments (Figure 6) showed that the concentration of Cu ions can be up to 3 times higher than Ag ions in the first 2 hours of exposure to the different media, however, due to the rapid oxidation of Cu, its bacterial inhibition activity period is shorter than Ag and therefore a higher concentration of Cu is needed to inhibit bacterial growth for 24 hours (Figure S2a, S2b) [52]. The agglomeration process observed in the pristine bimetallic NPs (Figure 3a) would reduce the reactive surface area and the ability to release ions, which results in a higher concentration of NPs needed to inhibit bacterial growth over time. The MIC of monometallic Cu and Ag NPs used in this study to inhibit *E. coli* growth was 400 $mg \cdot L^{-1}$ and 10 $mg \cdot L^{-1}$, respectively (Figure S2). Comparing these results with the net concentration of Cu and Ag used to inhibit bacterial growth by bimetallic NPs (Table 2), we observed that the MIC values were only 16.8 $mg \cdot L^{-1}$ and 8.2 $mg \cdot L^{-1}$ of Cu and Ag, respectively, for the same strain of *E. coli*. According to these results, Ag NPs would be the main inhibitor of bacterial growth both in the presence and absence of Cu NPs. The antibacterial activity of Ag NPs is widely known, and the inhibition concentration can vary depending on the physicochemical properties of NPs [53–56]. However, the NP

concentration range used in this study did not allow us to evaluate the minimum NP concentration that would determine the antibacterial activity difference between bimetallic NPs and Ag NPs.

The three aluminosilicate geomaterials studied did not present antibacterial action by themselves, as has been pointed out in earlier studies [57–59]. However, the intrinsic characteristics of the geomaterials governed the release capacity of the supported NPs, as well as the way of direct interaction of the NPs with the studied bacteria, based on the degree of agglomeration of the NPs on the support matrix as well as the overall charge and stability of the Geomat_Cu/Ag composite. The Minimum Inhibitory Concentrations of the different Geomat_Cu/Ag composites is shown on Table 2 for *E. coli* and *S. aureus*

Table 2. Minimum Inhibitory Concentration at 24 h (MIC) and net Cu and Ag concentration used to inhibit the growth of *E. coli* and *S. aureus*.

Materials	**MIC** **(mg · L^{-1})**		**Net concentration of metal** **(mg · L^{-1})**			
	E. coli	*S. aureus*	*E. coli*		*S. aureus*	
			Cu	Ag	Cu	Ag
Cu/Ag NPs	25	25	16.8	8.2	16.8	8.2
Cu/Ag_Imo	50	100	15.1	4.6	30.1	9.3
Cu/Ag_Mtt	25	50	8.3	3.2	16.7	6.4
Cu/Ag_Zeo	6.25	6.25	2.2	0.9	2.2	0.9

For Imo_Cu/Ag, the bacterial growth graphs show that, during the first 6 h, a material concentration of 25 mg·L^{-1} inhibited growth by 99% (Fig 6a, 6b), the same material at 6 h of

exposure in MHB medium releases ~10% Cu and Ag supported on Imo (Figure 6c, 6d). However, the slowdown of metal release from Imo-supported NPs, due to the uneven distribution of NPs on the surface and the agglomeration of NPs at the edges of the Imo nanotubes, decreased the antibacterial efficacy of the composite over time. The increase of Cu and Ag ions release from Imo_Cu/Ag between 2 h and 24 h in HMB was the lowest of the three Geo_NPs, with 14% and 30% for Cu and Ag, respectively. The inhibition of bacterial growth at 24 h for Imo_Cu/Ag would therefore be mainly from the direct contact of the composite with the bacteria. The dose necessary of composite to inhibit 99% of bacterial growth at 24 h was 50 $mg \cdot L^{-1}$ for *E. coli* and 100 $mg \cdot L^{-1}$ for *S. aureus* (Figure 7c, 7d). Table 2 shows the relationship between MIC and the proportional concentration of Cu and Ag in each material (Table 1), which is explained by Eq 1, which allowed to determine the net concentration of Cu and Ag alone needed to inhibit each bacterial strain. The net concentration of Cu+Ag in the Imo_Cu/Ag composite (measured from ICP-AES data) required to inhibit *E. coli* growth at 24 h was half that of Cu+Ag used for *S. aureus* (Table 2).

The distribution of Cu/Ag NPs on the Mtt surface allowed for a higher active surface area and higher metal release over time [60]. At the end of 24 h, ~12% of total Cu and ~17% of total Ag was released from the Mtt_Cu/Ag composite (Figure 6 c and d). During the initial hours of exposure, the growth inhibition would be mediated by ion release and direct contact of bacteria with the composite whereas, after 12 h, the rate of metal release decreased and growth inhibition would be mainly due to physical Mtt_Cu/Ag-bacteria interactions [61]. In the first 12 h, the necessary concentration that prevented the growth of both strains was 25 $mg \cdot L^{-1}$ of Mtt_Cu/Ag, a concentration that was maintained until 24 h only for *E. coli* (Figure 7 e and f; Table 2). Previous studies showed that the interaction of Mtt and Cu or Ag NPs could cause an increase in their

surface charge, increasing the adsorption capacity on bacteria, especially those with a negative charge in their cell wall, such as *E. coli* [62,63], due to lower electrostatic repulsion.

For Zeo_Cu/Ag, the release efficiency of Cu and Ag ions in the MHB medium at 24 h was ~14% total Cu and 20% total Ag contained in this composite (Figure 6c, 6d). The SiO_2/Al_2O_3 ratio in the Zeo structure [64], together with the stability of Zeo in a wide pH range (Figure 5a, 5b), allowed high retention and stabilization of NPs in the Zeo structure. Zeo materials also release metal ions through ion exchange and dissolution mechanisms, which made them excellent support for biocidal NPs [65,66]. This compound, moreover, shows the highest Ag concentration and a lower Cu/Ag ratio (2.58) with respect to the other Geomat_Cu/Ag compounds (Table 1 and 2). These characteristics allowed Zeo_Cu/Ag to inhibit the growth of *E. coli* and *S. aureus* at the lowest material concentration applied (6.25 $mg \cdot L^{-1}$) (Figure 7 g and h; Table 2), which correspond to a metal concentration of 3.1 $mg \cdot L^{-1}$ for this composite (corresponding to ~36% Cu NPs and ~14% Ag NPs (Table 2). Therefore, Zeo was the best support material for the synthesis of Geomat_Cu/Ag antibacterial composites, requiring up to ~180-fold less Cu and ~11-fold less Ag than monometallic NPs for inhibiting the same bacterial strains.

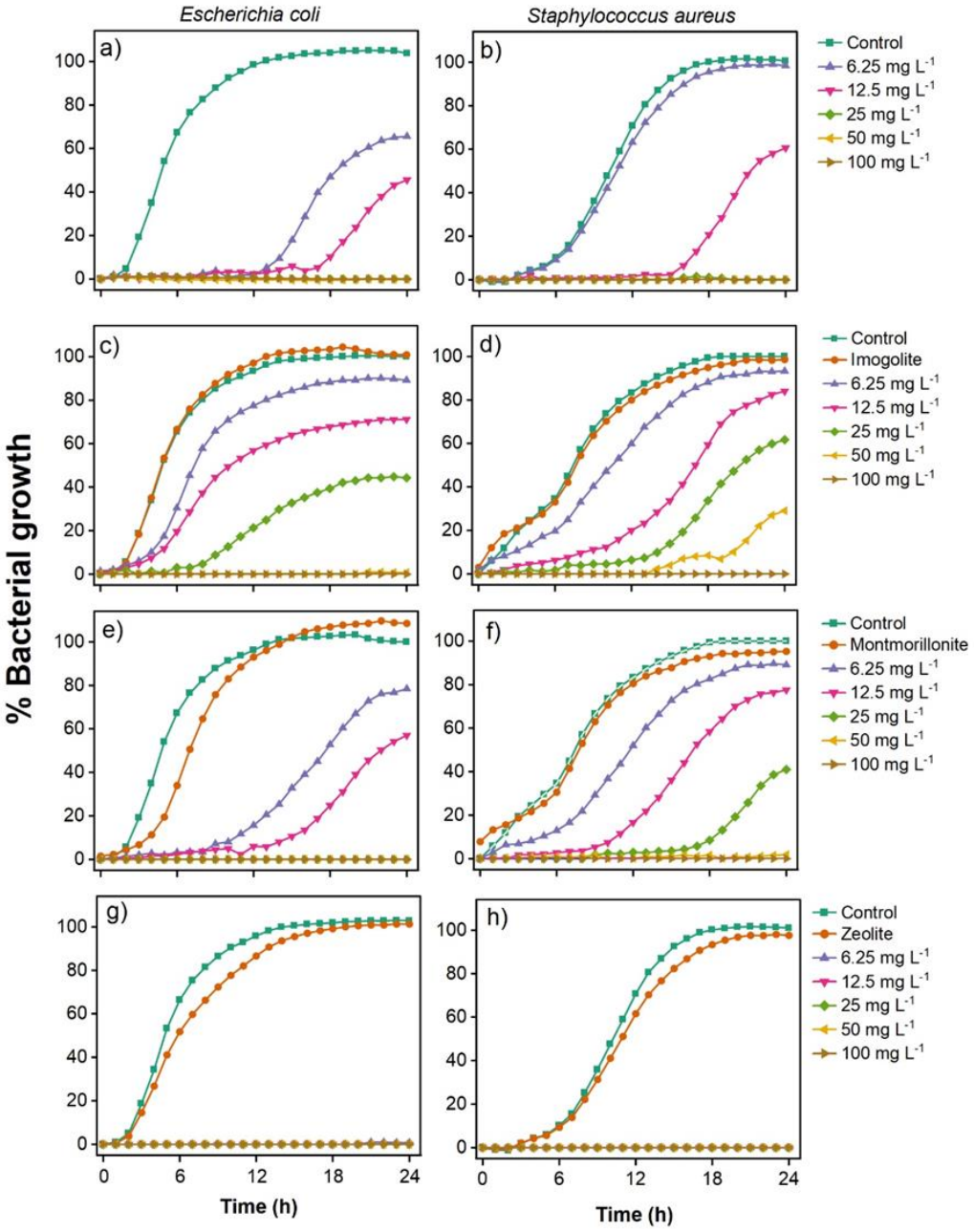

Figure 7. Effect of Cu/Ag NPs (a, b), composites Imo_Cu/Ag (c, d), Mtt_Cu/Ag (e, f) and Zeo_Cu/Ag (g, h) in the percentage of bacterial growth of *Escherichia coli* and *Staphylococcus aureus* over 24 h at the concentration of 6.25, 12.5, 25, 50, 100 mg·L^{-1} and geomaterial alone at 200 mg·L^{-1}.

4. Conclusions

The Cu/Ag bimetallic NPs alone or NPs supported on aluminosilicate geomaterials caused some degree of antibacterial effect, by inhibiting, retarding or decreasing the final growth rate of *E. coli* and *A. aureus*. The antibacterial efficacy of the bimetallic NPs was associated both to their physicochemical characteristics, such as the degree of oxidation and agglomeration of the bimetallic NPs, and their coordination with the aluminosilicate geomaterials used as support. The use of geomaterials as support for bimetallic NPs allowed to increase the contact surface area of NPs, avoiding agglomeration and increasing the release of Cu and Ag ions, which improved their antibacterial activity. Results of this work highlighted differences of antibacterial activity provided by bimetallic NPs in relation to the morphology and chemical reactivity of various geomaterials. The Zeo was identified as the best immobilization support for Cu/Ag NPs. The surface charge of Zeo allowed a homogeneous distribution of the NPs on its surface, increasing the reactive area of these NPs due to low agglomeration and low metal oxidation. This resulted in a more controlled release of Cu and Ag metal ions to the medium and improve the antibacterial effect over time. This study synthesized composites doped with high percentage of NPs (~40%) which allowed the use of relatively low concentrations of the material for antibacterial applications. Therefore, this material shows clear advantages for its use as antibacterial agent to inactivate pathogen or control microbial growth in environmental or biomedical applications.

Supporting Information

- Figure S1. SEM images and EDS spectra of (a) Cu/Ag bimetallic NPs, (b) Imo_Cu/Ag, (c) Mtt_Cu/Ag and (d) Zeo_Cu/Ag.

- Figure S2. Effect of Cu (a) and Ag (b) NPs on the growth of *Escherichia coli* over 24 h at particle concentrations of 10, 50, 100, 200, 300 and 400 $mg \cdot L^{-1}$.
- Table S1. Minimum inhibitory concentration at 24 h (MIC) for E. coli in relation to different percentages of Ag and Cu used for the synthesis of bimetallic NPs.

Acknowledgments

The authors thank Plan de Fortalecimiento de Universidades Estatales (ATA20992). This study was supported by the FONDECYT Grants No. 11171079 and Basal Funding for Scientific and Technological Centers under Project AFB 180001 CEDENNA to E.C. B.S. was supported by the Lancaster Environment Centre Project.

References

(1) Hudson-Smith, N. V.; Clement, P. L.; Brown, R. P.; Krause, M. O. P.; Pedersen, J. A.; Haynes, C. L. Research Highlights: Speciation and Transformations of Silver Released from Ag NPs in Three Species. *Environ. Sci. Nano* **2016**, *3* (6), 1236–1240. https://doi.org/10.1039/c6en90025a.

(2) Balasubramaniam, B.; Prateek; Ranjan, S.; Saraf, M.; Kar, P.; Singh, S. P.; Thakur, V. K.; Singh, A.; Gupta, R. K. Antibacterial and Antiviral Functional Materials: Chemistry and Biological Activity toward Tackling COVID-19-like Pandemics. *ACS Pharmacol. Transl. Sci.* **2021**, *4* (1), 8–54. https://doi.org/10.1021/acsptsci.0c00174.

(3) Godoy-Gallardo, M.; Eckhard, U.; Delgado, L. M.; de Roo Puente, Y. J. D.; Hoyos-Nogués, M.; Gil, F. J.; Perez, R. A. Antibacterial Approaches in Tissue Engineering Using Metal Ions and Nanoparticles: From Mechanisms to Applications. *Bioact. Mater.* **2021**, *6*

(12), 4470–4490. https://doi.org/10.1016/j.bioactmat.2021.04.033.

(4) Stabryla, L. M.; Johnston, K. A.; Millstone, J. E.; Gilbertson, L. M. Emerging Investigator Series: It's Not All about the Ion: Support for Particle-Specific Contributions to Silver Nanoparticle Antimicrobial Activity. *Environ. Sci. Nano* **2018**, *5* (9), 2047–2068. https://doi.org/10.1039/c8en00429c.

(5) Abebe, B.; Zereffa, E. A.; Murthy, H. C. A. Synthesis of Poly(Vinyl Alcohol)-Aided ZnO/Mn2O3Nanocomposites for Acid Orange-8 Dye Degradation: Mechanism and Antibacterial Activity. *ACS Omega* **2021**, *6* (1), 954–964. https://doi.org/10.1021/acsomega.0c05597.

(6) Sánchez-López, E.; Gomes, D.; Esteruelas, G.; Bonilla, L.; Lopez-Machado, A. L.; Galindo, R.; Cano, A.; Espina, M.; Ettcheto, M.; Camins, A.; Silva, A. M.; Durazzo, A.; Santini, A.; Garcia, M. L.; Souto, E. B. Metal-Based Nanoparticles as Antimicrobial Agents: An Overview. *Nanomaterials* **2020**, *10* (2), 1–39. https://doi.org/10.3390/nano10020292.

(7) Slavin, Y. N.; Asnis, J.; Häfeli, U. O.; Bach, H. Metal Nanoparticles: Understanding the Mechanisms behind Antibacterial Activity. *J. Nanobiotechnology* **2017**, *15* (1), 1–20. https://doi.org/10.1186/s12951-017-0308-z.

(8) Fatima, F.; Siddiqui, S.; Khan, W. A. Nanoparticles as Novel Emerging Therapeutic Antibacterial Agents in the Antibiotics Resistant Era. *Biol. Trace Elem. Res.* **2021**, *199* (7), 2552–2564. https://doi.org/10.1007/s12011-020-02394-3.

(9) Gholami, M.; Azarbani, F.; Hadi, F.; Murthy, H. C. A. Eco-Friendly Synthesis of Copper Nanoparticles Using Mentha Pulegium Leaf Extract: Characterisation, Antibacterial and Cytotoxic Activities. *Mater. Technol.* **2021**, *00* (00), 1–9.

https://doi.org/10.1080/10667857.2021.1959214.

(10) Ermini, M. L.; Voliani, V. Antimicrobial Nano-Agents: The Copper Age. *ACS Nano* **2021**, *15* (4), 6008–6029. https://doi.org/10.1021/acsnano.0c10756.

(11) Tambosi, R.; Liotenberg, S.; Bourbon, M. L.; Steunou, A. S.; Babot, M.; Durand, A.; Kebaili, N.; Ouchane, S. Silver and Copper Acute Effects on Membrane Proteins and Impact on Photosynthetic and Respiratory Complexes in Bacteria. *MBio* **2018**, *9* (6), 1–13. https://doi.org/10.1128/mBio.01535-18.

(12) Murthy, H. C. A.; Desalegn, T.; Kassa, M.; Abebe, B.; Assefa, T. Synthesis of Green Copper Nanoparticles Using Medicinal Plant Hagenia Abyssinica (Brace) JF . Gmel . Leaf Extract : Antimicrobial Properties. **2020**, *2020*.

(13) Fan, X.; Yahia, L.; Sacher, E. Antimicrobial Properties of the Ag, Cu Nanoparticle System. *Biology (Basel).* **2021**, *10* (2), 1–37. https://doi.org/10.3390/biology10020137.

(14) Kaweeteerawat, C.; Chang, C. H.; Roy, K. R.; Liu, R.; Li, R.; Toso, D.; Fischer, H.; Ivask, A.; Ji, Z.; Zink, J. I.; Zhou, Z. H.; Chanfreau, G. F.; Telesca, D.; Cohen, Y.; Holden, P. A.; Nel, A. E.; Godwin, H. A. Cu Nanoparticles Have Different Impacts in Escherichia Coli and Lactobacillus Brevis than Their Microsized and Ionic Analogues. *ACS Nano* **2015**, *9* (7), 7215–7225. https://doi.org/10.1021/acsnano.5b02021.

(15) Lee, C.; Kim, N. R.; Koo, J.; Lee, Y. J.; Lee, H. M. Cu-Ag Core-Shell Nanoparticles with Enhanced Oxidation Stability for Printed Electronics. *Nanotechnology* **2015**, *26* (45), 455601. https://doi.org/10.1088/0957-4484/26/45/455601.

(16) Perdikaki, A.; Galeou, A.; Pilatos, G.; Karatasios, I.; Kanellopoulos, K.; Prombona, A.; Karanikolos, G. N. Ag and Cu Monometallic and Ag / Cu Bimetallic Nanoparticle - Graphene Composites with Enhanced Antibacterial Performance Ag and Cu

Monometallic and Ag / Cu Bimetallic Nanoparticle - Graphene Composites with Enhanced Antibacterial Performance. **2016**. https://doi.org/10.1021/acsami.6b08403.

(17) Ferrando, R.; Jellinek, J.; Johnston, R. L. Nanoalloys: From Theory to Applications of Alloy Clusters and Nanoparticles. *Chem. Rev.* **2008**, *108* (3), 845–910. https://doi.org/10.1021/cr040090g.

(18) Zhang, S.; Nguyen, L.; Liang, J. X.; Shan, J.; Liu, J. J.; Frenkel, A. I.; Patlolla, A.; Huang, W.; Li, J.; Tao, F. F. Catalysis on Singly Dispersed Bimetallic Sites. *Nat. Commun.* **2015**, *6*, 1–10. https://doi.org/10.1038/ncomms8938.

(19) Yang, G.; Zou, Q.; Wang, P.; Lai, H.; Lai, T.; Zeng, X.; Li, Z.; Luo, J.; Zhang, Y.; Cui, C. Towards Understanding the Facile Synthesis of Well-Covered Cu-Ag Core-Shell Nanoparticles from a Complexing Model. *J. Alloys Compd.* **2021**, *874*, 159900. https://doi.org/10.1016/j.jallcom.2021.159900.

(20) Wang, D.; Liu, J.; Xi, J.; Jiang, J.; Bai, Z. Pd-Fe Dual-Metal Nanoparticles Confined in the Interface of Carbon Nanotubes/N-Doped Carbon for Excellent Catalytic Performance. *Appl. Surf. Sci.* **2019**, *489* (May), 477–484. https://doi.org/10.1016/j.apsusc.2019.06.039.

(21) Zhang, N.; Qiu, Y.; Sun, H.; Hao, J.; Chen, J.; Xi, J.; Liu, J.; He, B.; Bai, Z. W. Substrate-Assisted Encapsulation of Pd-Fe Bimetal Nanoparticles on Functionalized Silica Nanotubes for Catalytic Hydrogenation of Nitroarenes and Azo Dyes. *ACS Appl. Nano Mater.* **2021**, *4* (6), 5854–5863. https://doi.org/10.1021/acsanm.1c00777.

(22) Motshekga, S. C.; Ray, S. S.; Onyango, M. S.; Momba, M. N. B. Microwave-Assisted Synthesis, Characterization and Antibacterial Activity of Ag/ZnO Nanoparticles Supported Bentonite Clay. *J. Hazard. Mater.* **2013**, *262*, 439–446. https://doi.org/10.1016/j.jhazmat.2013.08.074.

(23) De Faria, A. F.; Perreault, F.; Shaulsky, E.; Arias Chavez, L. H.; Elimelech, M. Antimicrobial Electrospun Biopolymer Nanofiber Mats Functionalized with Graphene Oxide-Silver Nanocomposites. *ACS Appl. Mater. Interfaces* **2015**, *7* (23), 12751–12759. https://doi.org/10.1021/acsami.5b01639.

(24) Schiffman, J. D.; Wang, Y.; Giannelis, E. P.; Elimelech, M. Biocidal Activity of Plasma Modified Electrospun Polysulfone Mats Functionalized with Polyethyleneimine-Capped Silver Nanoparticles. *Langmuir* **2011**, *27* (21), 13159–13164. https://doi.org/10.1021/la202605z.

(25) Moradpoor, H.; Safaei, M.; Mozaffari, H. R.; Sharifi, R.; Imani, M. M.; Golshah, A.; Bashardoust, N. An Overview of Recent Progress in Dental Applications of Zinc Oxide Nanoparticles. *RSC Adv.* **2021**, *11* (34), 21189–21206. https://doi.org/10.1039/d0ra10789a.

(26) Jayrajsinh, S.; Shankar, G.; Agrawal, Y. K.; Bakre, L. Montmorillonite Nanoclay as a Multifaceted Drug-Delivery Carrier: A Review. *J. Drug Deliv. Sci. Technol.* **2017**, *39*, 200–209. https://doi.org/10.1016/j.jddst.2017.03.023.

(27) Kaushik, M.; Moores, A. Review: Nanocelluloses as Versatile Supports for Metal Nanoparticles and Their Applications in Catalysis. *Green Chem.* **2016**, *18* (3), 622–637. https://doi.org/10.1039/c5gc02500a.

(28) Ma, W.; Soroush, A.; Luong, T. V. A.; Rahaman, M. S. Cysteamine- and Graphene Oxide-Mediated Copper Nanoparticle Decoration on Reverse Osmosis Membrane for Enhanced Anti-Microbial Performance. *J. Colloid Interface Sci.* **2017**, *501*, 330–340. https://doi.org/10.1016/j.jcis.2017.04.069.

(29) Soroush, A.; Ma, W.; Cyr, M.; Rahaman, M. S.; Asadishad, B.; Tufenkji, N. In Situ Silver

Decoration on Graphene Oxide-Treated Thin Film Composite Forward Osmosis Membranes: Biocidal Properties and Regeneration Potential. *Environ. Sci. Technol. Lett.* **2016**, *3* (1), 13–18. https://doi.org/10.1021/acs.estlett.5b00304.

(30) Chen, S.; Popovich, J.; Zhang, W.; Ganser, C.; Haydel, S. E.; Seo, D. K. Superior Ion Release Properties and Antibacterial Efficacy of Nanostructured Zeolites Ion-Exchanged with Zinc, Copper, and Iron. *RSC Adv.* **2018**, *8* (66), 37949–37957. https://doi.org/10.1039/C8RA06556J.

(31) Kim, Y. H.; Lee, D. K.; Cha, H. G.; Kim, C. W.; Kang, Y. S. Synthesis and Characterization of Antibacterial Ag - SiO2 Nanocomposite. *J. Phys. Chem. C* **2007**, *111* (9), 3629–3635. https://doi.org/10.1021/jp068302w.

(32) Dutta, P.; Wang, B. Zeolite-Supported Silver as Antimicrobial Agents. *Coord. Chem. Rev.* **2019**, *383*, 1–29. https://doi.org/10.1016/j.ccr.2018.12.014.

(33) Arancibia-Miranda, N.; Baltazar, S. E.; García, A.; Muñoz-Lira, D.; Sepúlveda, P.; Rubio, M. A.; Altbir, D. Nanoscale Zero Valent Supported by Zeolite and Montmorillonite: Template Effect of the Removal of Lead Ion from an Aqueous Solution. *J. Hazard. Mater.* **2016**, *301*, 371–380. https://doi.org/10.1016/j.jhazmat.2015.09.007.

(34) Arancibia-Miranda, N.; Escudey, M. *Imogolite-Like Family*, 1st ed.; Elsevier Ltd., 2016; Vol. 7. https://doi.org/10.1016/B978-0-08-100293-3.00019-4.

(35) Arancibia-Miranda, N.; Escudey, M.; Molina, M.; García-González, M. T. Use of Isoelectric Point and PH to Evaluate the Synthesis of a Nanotubular Aluminosilicate. *J. Non. Cryst. Solids* **2011**, *357* (7), 1750–1756. https://doi.org/10.1016/j.jnoncrysol.2011.01.012.

(36) Adeleye, A. S.; Oranu, E. A.; Tao, M.; Keller, A. A. Release and Detection of Nanosized

Copper from a Commercial Antifouling Paint. *Water Res.* **2016**, *102*, 374–382. https://doi.org/10.1016/j.watres.2016.06.056.

(37) Sepúlveda, P.; Rubio, M. A.; Baltazar, S. E.; Rojas-Nunez, J.; Sánchez Llamazares, J. L.; Garcia, A. G.; Arancibia-Miranda, N. As(V) Removal Capacity of FeCu Bimetallic Nanoparticles in Aqueous Solutions: The Influence of Cu Content and Morphologic Changes in Bimetallic Nanoparticles. *J. Colloid Interface Sci.* **2018**, *524*, 177–187. https://doi.org/10.1016/j.jcis.2018.03.113.

(38) Ghadiri, M.; Chrzanowski, W.; Rohanizadeh, R. Biomedical Applications of Cationic Clay Minerals. *RSC Adv.* **2015**, *5* (37), 29467–29481. https://doi.org/10.1039/c4ra16945j.

(39) Krishnan, B.; Mahalingam, S. Ag/TiO2/Bentonite Nanocomposite for Biological Applications: Synthesis, Characterization, Antibacterial and Cytotoxic Investigations. *Adv. Powder Technol.* **2017**, *28* (9), 2265–2280. https://doi.org/10.1016/j.apt.2017.06.007.

(40) Roy, A.; Joshi, M.; Butola, B. S.; Malhotra, S. Antimicrobial and Toxicological Behavior of Montmorillonite Immobilized Metal Nanoparticles. *Mater. Sci. Eng. C* **2018**, *93* (July), 704–715. https://doi.org/10.1016/j.msec.2018.08.029.

(41) Arancibia-Miranda, N.; Silva-Yumi, J.; Escudey, M. Effect of Cations in the Background Electrolyte on the Adsorption Kinetics of Copper and Cadmium and the Isoelectric Point of Imogolite. *J. Hazard. Mater.* **2015**, *299*, 675–684. https://doi.org/10.1016/j.jhazmat.2015.08.007.

(42) Kang, H. Y.; Peng, C. Y.; Wang, H. P.; Lin, W. K.; Sun, I. W.; Chang, S. G. Preparation of Ag Nanospheres Filled with Cu. *J. Exp. Nanosci.* **2015**, *10* (12), 937–946. https://doi.org/10.1080/17458080.2014.938316.

(43) Ipek Yucelen, G.; Connell, R. E.; Terbush, J. R.; Westenberg, D. J.; Dogan, F. Synthesis

and Immobilization of Silver Nanoparticles on Aluminosilicate Nanotubes and Their Antibacterial Properties. *Appl. Nanosci.* **2016**, *6* (4), 607–614. https://doi.org/10.1007/s13204-015-0467-x.

(44) Clarke, C. J.; McBride, M. B. Cation and Anion Retention by Natural and Synthetic Allophane and Imogolite. *Clays Clay Miner.* **1984**, *32* (4), 291–299. https://doi.org/10.1346/ccmn.1984.0320407.

(45) Arancibia-Miranda, N.; Manquián-Cerda, K.; Pizarro, C.; Maldonado, T.; Suazo-Hernández, J.; Escudey, M.; Bolan, N.; Sarkar, B. Mechanistic Insights into Simultaneous Removal of Copper, Cadmium and Arsenic from Water by Iron Oxide-Functionalized Magnetic Imogolite Nanocomposites. *J. Hazard. Mater.* **2020**, *398* (May), 122940. https://doi.org/10.1016/j.jhazmat.2020.122940.

(46) Suazo-Hernández, J.; Sepúlveda, P.; Manquián-Cerda, K.; Ramírez-Tagle, R.; Rubio, M. A.; Bolan, N.; Sarkar, B.; Arancibia-Miranda, N. Synthesis and Characterization of Zeolite-Based Composites Functionalized with Nanoscale Zero-Valent Iron for Removing Arsenic in the Presence of Selenium from Water. *J. Hazard. Mater.* **2019**, *373* (March), 810–819. https://doi.org/10.1016/j.jhazmat.2019.03.125.

(47) Paineau, E.; Amara, M. S.; Monet, G.; Peyre, V.; Rouzière, S.; Launois, P. Effect of Ionic Strength on the Bundling of Metal Oxide Imogolite Nanotubes. *J. Phys. Chem. C* **2017**, *121* (39), 21740–21749. https://doi.org/10.1021/acs.jpcc.7b07391.

(48) Varadwaj, G. B. B.; Parida, K. M. Montmorillonite Supported Metal Nanoparticles: An Update on Syntheses and Applications. *RSC Adv.* **2013**, *3* (33), 13583–13593. https://doi.org/10.1039/c3ra40520f.

(49) Bai, R.; Song, Y.; Li, Y.; Yu, J. Creating Hierarchical Pores in Zeolite Catalysts. *Trends*

Chem. **2019**, *1* (6), 601–611. https://doi.org/10.1016/j.trechm.2019.05.010.

(50) Sathya, S.; Murthy, P. S.; Das, A.; Gomathi Sankar, G.; Venkatnarayanan, S.; Pandian, R.; Sathyaseelan, V. S.; Pandiyan, V.; Doble, M.; Venugopalan, V. P. Marine Antifouling Property of PMMA Nanocomposite Films: Results of Laboratory and Field Assessment. *Int. Biodeterior. Biodegrad.* **2016**, *114*, 57–66. https://doi.org/10.1016/j.ibiod.2016.05.026.

(51) Tang, S.; Zheng, J. Antibacterial Activity of Silver Nanoparticles: Structural Effects. *Adv. Healthc. Mater.* **2018**, *7* (13), 1–10. https://doi.org/10.1002/adhm.201701503.

(52) Tamayo, L.; Azócar, M.; Kogan, M.; Riveros, A.; Páez, M. Copper-Polymer Nanocomposites: An Excellent and Cost-Effective Biocide for Use on Antibacterial Surfaces. *Mater. Sci. Eng. C* **2016**, *69*, 1391–1409. https://doi.org/10.1016/j.msec.2016.08.041.

(53) Hajipour, M. J.; Fromm, K. M.; Akbar Ashkarran, A.; Jimenez de Aberasturi, D.; Larramendi, I. R. de; Rojo, T.; Serpooshan, V.; Parak, W. J.; Mahmoudi, M. Antibacterial Properties of Nanoparticles. *Trends Biotechnol.* **2012**, *30* (10), 499–511. https://doi.org/10.1016/j.tibtech.2012.06.004.

(54) Marambio-Jones, C.; Hoek, E. M. V. A Review of the Antibacterial Effects of Silver Nanomaterials and Potential Implications for Human Health and the Environment. *J. Nanoparticle Res.* **2010**, *12* (5), 1531–1551. https://doi.org/10.1007/s11051-010-9900-y.

(55) Peron, S.; Hadi, F.; Azarbani, F.; Ananda Murthy, H. C. Antimicrobial, Antioxidant, Anti-Glycation and Toxicity Studies on Silver Nanoparticles Synthesized Using Rosa Damascena Flower Extract. *Green Chem. Lett. Rev.* **2021**, *14* (3), 518–532. https://doi.org/10.1080/17518253.2021.1963492.

(56) Desalegn, T.; Ananda, C. R. R. H. C. Eco - Friendly Synthesis of Silver Nanostructures

Using Medicinal Plant Vernonia Amygdalina Del . Leaf Extract for Multifunctional Applications. *Appl. Nanosci.* **2020**, No. 0123456789. https://doi.org/10.1007/s13204-020-01620-7.

(57) Hu, C. H.; Xu, Z. R.; Xia, M. S. Antibacterial Effect of Cu2+-Exchanged Montmorillonite on Aeromonas Hydrophila and Discussion on Its Mechanism. *Vet. Microbiol.* **2005**, *109* (1–2), 83–88. https://doi.org/10.1016/j.vetmic.2005.04.021.

(58) Avellan, A.; Levard, C.; Rose, J.; Auffan, M.; Bertrand, M.; Olivi, L.; Santaella, C.; Achouak, W.; Masion, A. Influence of Structural Defects of Ge-Imogolite Nanotubes on Their Toxicity towards: Pseudomonas Brassicacearum. *Environ. Sci. Nano* **2016**, *3* (4), 839–846. https://doi.org/10.1039/c6en00060f.

(59) Abed, S.; Bakhsheshi-Rad, H. R.; Yaghoubi, H.; Ning, L.; Sadeghianmaryan, A.; Chen, X. Antibacterial Activities of Zeolite/Silver-Graphene Oxide Nanocomposite in Bone Implants. *Mater. Technol.* **2020**, *00* (00), 1–10. https://doi.org/10.1080/10667857.2020.1786784.

(60) Roy, A.; Butola, B. S.; Joshi, M. Synthesis, Characterization and Antibacterial Properties of Novel Nano-Silver Loaded Acid Activated Montmorillonite. *Appl. Clay Sci.* **2017**, *146* (February), 278–285. https://doi.org/10.1016/j.clay.2017.05.043.

(61) Bagchi, B.; Kar, S.; Dey, S. K.; Bhandary, S.; Roy, D.; Mukhopadhyay, T. K.; Das, S.; Nandy, P. In Situ Synthesis and Antibacterial Activity of Copper Nanoparticle Loaded Natural Montmorillonite Clay Based on Contact Inhibition and Ion Release. *Colloids Surfaces B Biointerfaces* **2013**, *108*, 358–365. https://doi.org/10.1016/j.colsurfb.2013.03.019.

(62) Gomes, C. F.; Gomes, J. H.; da Silva, E. F. Bacteriostatic and Bactericidal Clays: An

Overview. *Environ. Geochem. Health* **2020**, *42* (11), 3507–3527. https://doi.org/10.1007/s10653-020-00628-w.

(63) Rezazadeh, N.; Kianvash, A. Preparation, Characterization, and Antibacterial Activity of Chitosan/Silicone Rubber Filled Zeolite, Silver, and Copper Nanocomposites against Pseudomonas Aeruginosa and Methicillin-Resistant Staphylococcus Aureus. *J. Appl. Polym. Sci.* **2021**, *138* (23), 1–8. https://doi.org/10.1002/app.50552.

(64) Demirci, S.; Ustaoğlu, Z.; Yilmazer, G. A.; Sahin, F.; Baç, N. Antimicrobial Properties of Zeolite-X and Zeolite-A Ion-Exchanged with Silver, Copper, and Zinc against a Broad Range of Microorganisms. *Appl. Biochem. Biotechnol.* **2014**, *172* (3), 1652–1662. https://doi.org/10.1007/s12010-013-0647-7.

(65) Sánchez, M. J.; Mauricio, J. E.; Paredes, A. R.; Gamero, P.; Cortés, D. Antimicrobial Properties of ZSM-5 Type Zeolite Functionalized with Silver. *Mater. Lett.* **2017**, *191*, 65–68. https://doi.org/10.1016/j.matlet.2017.01.039.

(66) Salim, M. M.; Malek, N. A. N. N. Characterization and Antibacterial Activity of Silver Exchanged Regenerated NaY Zeolite from Surfactant-Modified NaY Zeolite. *Mater. Sci. Eng. C* **2016**, *59*, 70–77. https://doi.org/10.1016/j.msec.2015.09.099.

TOC Graphic

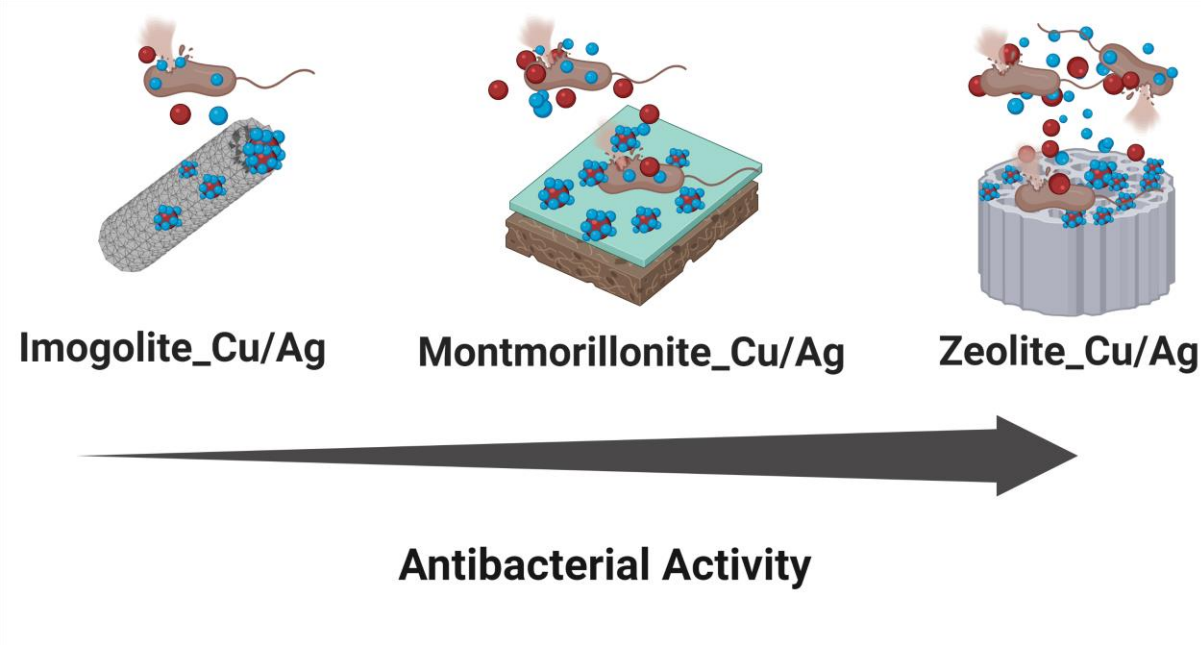
Imogolite_Cu/Ag
Montmorillonite_Cu/Ag
Zeolite_Cu/Ag
Antibacterial Activity

Supplementary Information:

Copper/Silver Bimetallic Nanoparticles Supported on Aluminosilicate Geomaterials as Antibacterial Agents

Edgardo Cruces[a,b]*, Nicolás Arancibia-Miranda[b,c], Karen Manquián-Cerda[c], François Perreault[d], Nanthi Bolan[e,f], Manuel Ignacio Azócar[c], Victor Cubillos[g], Jaime Montory[h], María Angélica Rubio[b,c], Binoy Sarkar[i]*

[a] Centro de Investigaciones Costeras Universidad de Atacama (CIC-UDA), Avenida Copayapu 485, Copiapó, Chile

[b] Center for the Development of Nanoscience and Nanotechnology, CEDENNA, 9170124, Santiago, Chile

[c] Facultad de Química y Biología, Universidad de Santiago de Chile, Av. B. O'Higgins, 363, Santiago, Chile

[d] School of Sustainable Engineering and the Built Environment, Arizona State University, Tempe, AZ, USA

[e] School of Agriculture and Environment, The University of Western Australia, Perth, WA 6001, Australia

[f] The UWA Institute of Agriculture, The University of Western Australia, Perth, WA 6001, Australia

[g] Instituto Ciencias Marinas y Limnológicas, Universidad Austral de Chile, Valdivia, Chile

[h] Centro i~mar, Universidad de Los Lagos, Casilla 557, Puerto Montt, Chile

[i] Lancaster Environment Centre, Lancaster University, Lancaster, LA1 4YQ, United Kingdom

*Corresponding authors: edgardo.cruces@usach.cl (E. Cruces)

b.sarkar@lancaster.ac.uk (B. Sarkar)

Supporting figures

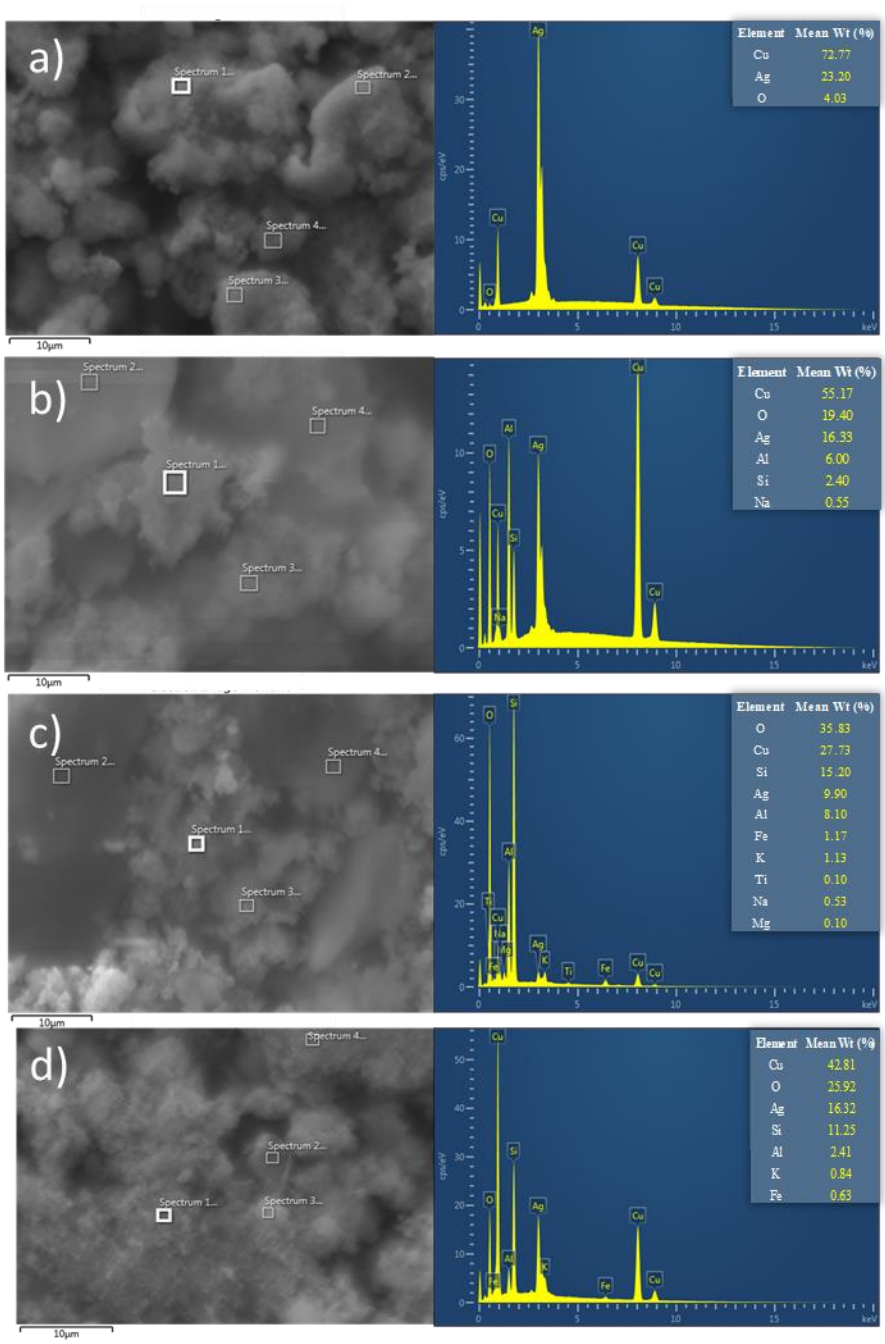

Figure S1. SEM images and EDS spectra of (a) Cu/Ag bimetallic NPs, (b) Imo_Cu/Ag, (c) Mtt_Cu/Ag and (d) Zeo_Cu/Ag.

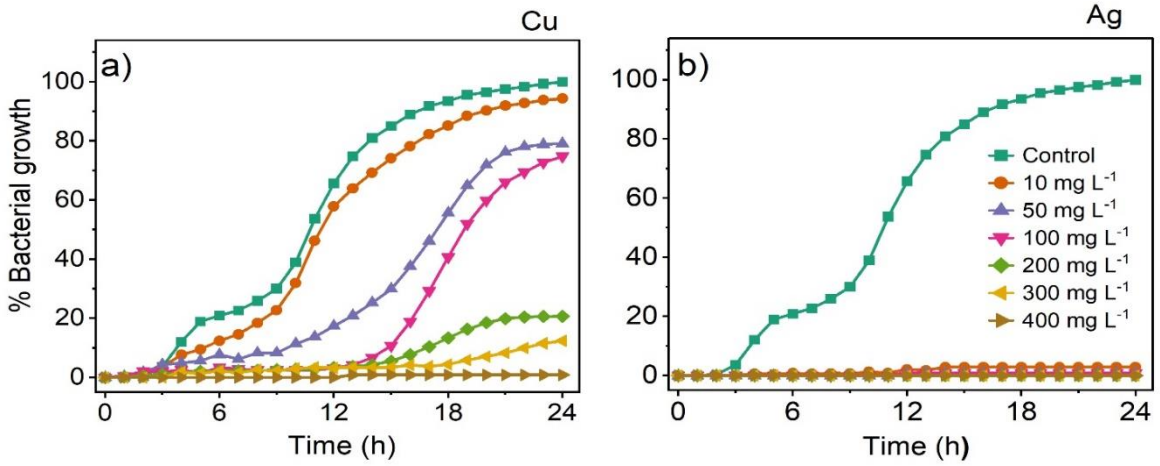

Figure S2. Effect of Cu (a) and Ag (b) NPs on the growth of *Escherichia coli* over 24 h at particle concentrations of 10, 50, 100, 200, 300 and 400 mg·L^{-1}. For the preparation of Cu and Ag NPs, to 1.0 mol·L^{-1} $CuCl_2 \cdot 6H_2O$ or $AgNO_3$ aqueous solution, 1.6 mol·L^{-1} $NaBH_4$ solution was added dropwise at room temperature under continuous mechanical stirring, according to Sepulveda et al (2018). The resulting solution was centrifuged at 9000 rpm for 10 min, and the supernatant was replaced with ethanol/water. To avoid oxidation of the NPs, an ethanol/water wash was performed, resulting in a fine powder product after lyophilization.

Supporting table

Table S1. Minimum inhibitory concentration at 24 h (MIC) for *E. coli* in relation to different percentages of Ag and Cu used for the synthesis of bimetallic NPs. Bimetallic NPs concentrations of 50, 75, 100, 150, 200 and 400 $mg \cdot L^{-1}$ were used for the determination (n=3).

Ag %	Cu %	MIC ($mg \cdot L^{-1}$)
5	95	400
10	90	200
15	85	150
20	80	100
25	75	100
30	70	75
35	65	50
40	60	50
45	55	50
50	50	50